Journal of Computational Physics 229 (2010) 1077–1098

Contents lists available at ScienceDirect

Journal of Computational Physics

journal homepage: www.elsevier.com/locate/jcp

A solution algorithm for the fluid dynamic equations based on a stochastic model for molecular motion

Patrick Jenny [a,*], Manuel Torrilhon [b], Stefan Heinz [c]

[a] Institute of Fluid Dynamics, ETH Zurich, Sonneggstrasse 3, CH-8092 Zurich, Switzerland
[b] Seminar for Applied Mathematics, ETH Zurich, Rämistrasse 101, CH-8092 Zurich, Switzerland
[c] Department of Mathematics, University of Wyoming, 1000 East University Avenue, Laramie, WY 82071, USA

ARTICLE INFO

Article history:
Received 27 January 2009
Received in revised form 7 October 2009
Accepted 7 October 2009
Available online 24 October 2009

Keywords:
Kinetic gas theory
Boltzman equation
Fokker–Planck equation
PDF methods
Monte-Carlo method
Stochastic differential equations

ABSTRACT

In this paper, a stochastic model is presented to simulate the flow of gases, which are not in thermodynamic equilibrium, like in rarefied or micro situations. For the interaction of a particle with others, statistical moments of the local ensemble have to be evaluated, but unlike in molecular dynamics simulations or DSMC, no collisions between computational particles are considered. In addition, a novel integration technique allows for time steps independent of the stochastic time scale.

The stochastic model represents a Fokker–Planck equation in the kinetic description, which can be viewed as an approximation to the Boltzmann equation. This allows for a rigorous investigation of the relation between the new model and classical fluid and kinetic equations. The fluid dynamic equations of Navier–Stokes and Fourier are fully recovered for small relaxation times, while for larger values the new model extents into the kinetic regime.

Numerical studies demonstrate that the stochastic model is consistent with Navier–Stokes in that limit, but also that the results become significantly different, if the conditions for equilibrium are invalid. The application to the Knudsen paradox demonstrates the correctness and relevance of this development, and comparisons with existing kinetic equations and standard solution algorithms reveal its advantages. Moreover, results of a test case with geometrically complex boundaries are presented.

1. Introduction

In this paper, a new stochastic modeling approach for monatomic gas flow is presented. The motivation is to improve our understanding regarding the applicability of the Navier–Stokes equation in situations with extreme gradients, e.g. in the presence of very strong shocks or micro-scale geometries. In these situations, lack of sufficient collisions between particles leads to strong non-equilibrium and the assumptions of the Navier–Stokes model are violated.

One way to address the validity of the Navier–Stokes equations is to use the concept of irreversible thermodynamics, where transport equations for the molecular stress tensor and heat flux are considered. This approach yields extended fluid dynamic models, which are successful, but still limited to moderate non-equilibrium, see e.g. [28,30] and references therein. Another approach is to use the equations of kinetic gas theory from which the equations for fluid- and thermodynamics can be derived. In general, the basis is provided by the Boltzmann equation, which is derived for rarefied gases and describes the evolution of the distribution function for particle velocities. The Boltzmann equation can be used in numerical computations

* Corresponding author. Tel.: +41 44 632 6987.
E-mail address: jenny@ifd.mavt.ethz.ch (P. Jenny).

0021-9991/$ - see front matter © 2009 Elsevier Inc. All rights reserved.
doi:10.1016/j.jcp.2009.10.008

by direct discretization. However, due to the high dimensionality of the distribution function and the complexity of the collision operator, the enormous computational requirements are a limiting factor.

Computational costs can be reduced by considering simplified models that replace Boltzmann's equation like the BGK model, see [20]. Still, in the BGK model an equation for the distribution function needs to be discretized. However, the collision operator is largely simplified. Another pragmatic procedure to solve the Boltzmann equation is given by the direct simulation Monte-Carlo (DSMC) method. In DSMC, particle paths and velocities are computed and local pair-wise collisions of the particles are introduced in a stochastic way. This method is successful, but only applicable for steady high speed flow problems; see [5].

In this paper, the approximation of the Boltzmann collision operator by a Fokker–Planck model, which was already published by Kirkwood [14,15] for liquids and by Heinz [9,10] for one-atomic gas, is analyzed and compared with other approximations. This Fokker–Planck model is proposed as an approach for monatomic gas flow, which may be viewed at the same time as a stochastic model for molecular motion. Moreover, a consistent and efficient numerical solution algorithm is devised. The mass density function (MDF) of molecules in the joint physical–velocity–space is consistently approximated by a cloud of stochastic particles, where the particle number density represents the mass density. Since the evolution of the particle positions and velocities by stochastic differential equations (SDEs) is relatively cheap, a very efficient and flexible numerical method can be derived. An important component is a novel time stepping scheme to integrate the SDEs for particle positions and velocities independent of the relaxation time. Note that this is crucial to also deal efficiently with very low Knudsen number flows, where the relaxation time (which scales linearly with the mean free path length) is typically much smaller than the time step size allowed by a simple CFL criterion. The method also features exact preservation of fluctuation energies. Since this particle algorithm is a consistent solution method for the Fokker–Planck equation, it can be employed to rigorously investigate the Fokker–Planck model in the context of kinetic gas theory. We would like to clarify that the goal of our method is to provide an approximation to the Boltzmann equation in a similar way as DSMC does.

It is easy to recognize the analogy of the stochastic model with probability density function (PDF) modeling of turbulent flows. The advantage of PDF methods is that both, convection and turbulence-reaction interaction are represented exactly without modeling assumptions [24]. They have successfully been applied in modeling several chemically inert [2,7,21] and reactive [22,18,26] flows. In terms of solution algorithms, particle methods are usually preferred, which is due to the high dimensionality of the PDF transport equation [13,12,25]. Although conceptually similar, here the algorithmic task is different. On one hand, there is no mean pressure coupling and on the other hand kinetic energy is conserved. In this paper we present a highly accurate, energy conserving particle tracking scheme, which is novel. Moreover, a consistent formulation of isothermal wall-boundary conditions is devised.

The strategy of this paper is the following: In Section 2, we formulate fundamental conditions for approximative models of Boltzmann's collision operator and derive the Fokker–Planck operator as such a model. Then, the accuracy of this model is investigated by studying the evolution equations of the fluid quantities induced by the model and by comparison to Boltzmann. After establishing the model, we transform the Fokker–Planck equation into stochastic differential equations for particle paths. Section 3 presents the discussion of the relation to other stochastic particle models and the comparison to DSMC. Section 4 derives the numerical method by exact integration of the stochastic equations with frozen coefficients for a full time step. Algorithmic details of how to extract and interpolate averaged quantities are given. In Section 5, we present numerical experiments that verify the preservation properties of the new method. Realistic cases like channel flow and two-dimensional external flow are investigated to demonstrate the capabilities of the new model.

2. Kinetic description of non-equilibrium gases

As the basis of our reasoning we assume that the statistics of particles in a gas can be described by the mass density function $\mathcal{F}(\boldsymbol{V},\boldsymbol{x},t)=\rho(\boldsymbol{x},t)f(\boldsymbol{V};\boldsymbol{x},t)$, where ρ is the gas density (particle number density times the single particle mass m) and f the probability density function (PDF) of the molecular velocity $\boldsymbol{M}$ at location $\boldsymbol{x}$ and time t. In equilibrium, the molecular velocity PDF is given by the Maxwell distribution $\mathcal{F}_M$

$$\mathcal{F}_M=\frac{\rho}{(2\pi kT/m)^{3/2}}\exp\left(-\frac{(V_i-U_i)^2}{2kT/m}\right), \tag{1}$$

which is constructed from the gas density ρ, the gas velocity $\boldsymbol{U}$ (mean molecular velocity) and the gas temperature T. The particles have mass m and k is the Boltzmann constant. Density, velocity and sensible energy $e_s=1.5kT/m$ follow from the mass density function (MDF) $\mathcal{F}$ by integration, i.e.

$$\left(\rho,\rho\boldsymbol{U},\rho e_s+\frac{1}{2}\rho\boldsymbol{U}^2\right)=\int_{\mathbb{R}^3}\boldsymbol{\Psi}_{\text{cons}}\mathcal{F}d\boldsymbol{V}=\int_{\mathbb{R}^3}\boldsymbol{\Psi}_{\text{cons}}\mathcal{F}_M d\boldsymbol{V} \tag{2}$$

with the weights $\boldsymbol{\Psi}_{\text{cons}}=(1,\boldsymbol{V},\frac{1}{2}\boldsymbol{V}^2)$. We define the fluctuation velocity of the particles by $\boldsymbol{u}=\boldsymbol{V}-\boldsymbol{U}$. With the relation $e_s=3/2\ k/m\ T$ we restrict ourselves to monatomic gases. In the following, we will also use the negative stress tensor p_{ij} and the heat flux q_i defined by

$$p_{ij}=\int_{\mathbb{R}^3}u_iu_j\mathcal{F}d\boldsymbol{V}\quad\text{and}\quad q_i=\int_{\mathbb{R}^3}\frac{1}{2}u_iu_ku_k\mathcal{F}d\boldsymbol{V} \tag{3}$$

for any MDF $\mathcal{F}$. Note that Einstein's summation convention is used throughout this paper. For abbreviation we write for the symmetric tracefree (deviatoric) part of a tensor $A_{\langle ij\rangle} = \frac{1}{2}(A_{ij} + A_{ji}) - \frac{1}{3}A_{kk}\delta_{ij}$, where δ_{ij} is the Kronecker symbol.

2.1. Kinetic equations

The evolution of $\mathcal{F}$ follows the kinetic equation

$$\frac{\partial \mathcal{F}}{\partial t} + V_i \frac{\partial \mathcal{F}}{\partial x_i} + \frac{\partial F_i \mathcal{F}}{\partial V_i} = S(\mathcal{F}), \tag{4}$$

where $\boldsymbol{F}$ is an external force, e.g. gravity. For simplicity, in this paper $\mathbf{F}$ is considered independent of $\boldsymbol{V}$. The left hand side of this equation describes the non-interacting free flight of the particles by means of a Liouville-operator for $\mathcal{F}$. The major modeling of the gas enters through the right hand side $S(\mathcal{F})$, which represents the particle interactions, i.e. the collisions. We formulate two fundamental properties of a general collision operator. Both are related to equilibrium, i.e.

$$\int_{\mathbb{R}^3} \boldsymbol{\Psi}_{\text{cons}} S(\mathcal{F}) d\boldsymbol{V} = 0 \quad \text{for any } \mathcal{F} \quad \text{and} \tag{5}$$

$$S(\mathcal{F}) = 0 \Rightarrow \mathcal{F} = \mathcal{F}_M. \tag{6}$$

Property (5) states that mass, momentum and energy are conserved during collisions, and property (6) states that a distribution is Maxwellian (in equilibrium), if it is not changed by the collisions. The modeling task of kinetic theory is to find an accurate and realistic expression for S.

Boltzmann's famous *Stosszahlansatz* leads to a collision operator of the form

$$S^{(\text{Boltz})}(\mathcal{F}) = \frac{1}{\rho} \int_{\mathbb{R}^5} g\ b(\mathcal{F}'(\boldsymbol{V})\mathcal{F}'(\boldsymbol{V}_1) - \mathcal{F}(\boldsymbol{V})\mathcal{F}(\boldsymbol{V}_1)) db d\varepsilon d\boldsymbol{V} \tag{7}$$

that describes the details of binary collisions in a dilute gas. Inside $S^{(\text{Boltz})}$ the MDFs $\mathcal{F}$ and $\mathcal{F}'$ of the velocities before and after a collision are evaluated; $g = |\boldsymbol{V} - \boldsymbol{V}_1|$ is the relative velocity, b the collision parameter and $\varepsilon \in [0, 2\pi]$ a collision angle. For details of this operator, see for example the book [6]. The Boltzmann equation can be solved numerically, however, full scale simulations are extremely expensive due to the discretization of the $\boldsymbol{x} - \boldsymbol{V} - t$ phase space and since the collision operator (7) has to be evaluated at every point of the phase space. It can easily be checked that the two properties (5) and (6) hold for the Boltzmann collision operator.

Many analytical and numerical evaluations demonstrate that the Boltzmann equation (4) with (7) indeed describes non-equilibrium gas dynamics accurately for a wide range of scenarios including rarefied gases and strong shocks. Extensions exist for very dense fluids and real gas effects. In this paper, we will consider the description given by the Boltzmann equation as a benchmark for our modeling approach of non-equilibrium gas flow.

To efficiently simulate non-equilibrium gases, the collision operator S is typically replaced by an expression simpler than the Boltzmann operator $S^{(\text{Boltz})}$. Ideally, such a model operator mimics as many properties of a realistic collision operator as possible, while still allowing efficient computations. First at all, it is natural to require that the two properties (5) and (6) are fulfilled. Second, if $S^{(\text{Boltz})}$ is the benchmark, it is also reasonable to aim for a match of further stochastic moment, i.e. that

$$\int_{\mathbb{R}^3} \boldsymbol{\Psi} S(\mathcal{F}) d\boldsymbol{V} = \int_{\mathbb{R}^3} \boldsymbol{\Psi} S^{(\text{Boltz})}(\mathcal{F}) d\boldsymbol{V} \tag{8}$$

for integration weights $\boldsymbol{\Psi} = (V_i V_j, V_i V_j V_k, \ldots, V_{i_1} V_{i_2} \cdots V_{i_N})$ of monomials of increasing degree. This property guarantees that the evolution equations of the model for the N moments $\int_{\mathbb{R}^3} \boldsymbol{\Psi}\mathcal{F} d\boldsymbol{V}$ are identical to the evolutions implied by the Boltzmann equation. Other conditions may include the existence of an entropy and other mathematical properties.

2.2. Collision models

The most popular collision model is the so-called BGK model [4]. This model can be derived from the Boltzmann operator by assuming that the post-collision velocities follow a Maxwell distribution, which allows to compute the integral in Eq. (7) explicitly. We find

$$S^{(\text{BGK})}(\mathcal{F}) = \frac{1}{\tau_{\text{BGK}}}(\mathcal{F}_M - \mathcal{F}), \tag{9}$$

which represents a relaxation towards the equilibrium $\mathcal{F}_M$ with relaxation time τ_{BGK}. Since $\mathcal{F}_M$ is an expression depending on density, velocity and temperature, $S^{(\text{BGK})}$ is still a non-linear integral operator for $\mathcal{F}$, although it appears as a simple expression. Obviously, $S^{(\text{BGK})}$ satisfies the equilibrium conditions (5) and (6). BGK has been used for many numerical computations, e.g. in [20].

The Boltzmann operator (7) can also be significantly simplified, if we assume small velocity changes through collisions. Note, that this assumption is to some extent similar to the assumption of BGK. With the assumption of small velocity

changes, the evaluation of the post-collision velocities in (7) can be linearized and with additional equilibrium assumptions the integrals become computable explicitly. For details, see [6]. The result is the Fokker–Planck operator

$$S^{(\mathrm{FP})}(\mathcal{F}) = \frac{\partial}{\partial V_i}\left(\frac{1}{\tau_{\mathrm{FP}}}(V_i - U_i)\mathcal{F}\right) + \frac{\partial^2}{\partial V_k \partial V_k}\left(\frac{2e_s}{3\tau_{\mathrm{FP}}}\mathcal{F}\right) \tag{10}$$

depending explicitly on the gas velocity $\boldsymbol{U}$, energy e_s and a relaxation time τ_{FP}. The Fokker–Planck operator can also be derived directly from particle motion, in particular for Brownian motion. However, here we want to stress the tight relation to the Boltzmann equation, i.e. we will focus on $S^{(\mathrm{FP})}$ as a Boltzmann model.

The main reason for replacing $S^{(\mathrm{Boltz})}$ by $S^{(\mathrm{FP})}$ is the possibility to use highly efficient numerical methods based on the stochastic description (see below). Already [6] states that expression (10) exhibits desirable properties to be used as a collision model. First of all, it satisfies the conditions (5) and (6), i.e. it obeys the conservation laws and ensures relaxation towards the equilibrium distribution $\mathcal{F}_M$. Similarly to $S^{(\mathrm{BGK})}$, it is not a linear operator, since velocity and energy appear in Eq. (10) as integrals of $\mathcal{F}$. However, in contrast to $S^{(\mathrm{BGK})}$, the non-linearity is quadratic, which is also the case for $S^{(\mathrm{Boltz})}$. Moreover, it can be shown that the Fokker–Planck operator is positive definite and represents a relaxation similar as Eq. (9) for small deviations $\mathcal{F} - \mathcal{F}_M$.

To demonstrate differences between the collision operators, we investigate property (8) for the moments of momentum and energy flux

$$P_{ij} = \int_{\mathbb{R}^3} u_i u_j S(\mathcal{F}) d\boldsymbol{V} \quad \text{and} \quad P_i = \int_{\mathbb{R}^3} \frac{1}{2} u_i u_k u_k S(\mathcal{F}) d\boldsymbol{V}, \tag{11}$$

respectively, which will be essential for the consistency with fluid dynamics. We find

$$\begin{aligned}
P_{ij}^{(\mathrm{Boltz})} &= -\alpha \frac{\rho}{m} p_{\langle ij\rangle}, \quad P_i^{(\mathrm{Boltz})} = -\frac{2}{3}\alpha \frac{\rho}{m} q_i, \\
P_{ij}^{(\mathrm{BGK})} &= -\frac{1}{\tau_{\mathrm{BGK}}} p_{\langle ij\rangle}, \quad P_i^{(\mathrm{BGK})} = -\frac{1}{\tau_{\mathrm{BGK}}} q_i, \\
P_{ij}^{(\mathrm{FP})} &= -\frac{2}{\tau_{\mathrm{FP}}} p_{\langle ij\rangle}, \quad P_i^{(\mathrm{FP})} = -\frac{3}{\tau_{\mathrm{FP}}} q_i,
\end{aligned} \tag{12}$$

where the Boltzmann result has been computed analytically for the interaction potential $\Phi(r) = \frac{\kappa}{4} r^{-4}$ (Maxwell molecules). The coefficient α is explicitly given by $\alpha = 4.11104\sqrt{\kappa/m}$. All models are linear in the pressure deviator $p_{\langle ij\rangle}$ and the heat flux q_i; differences are present in the factors, however. Obviously, $\alpha\rho/m$ has to be identified with an inverse relaxation time $\tau_{\mathrm{Boltz}} = (\alpha\rho/m)^{-1}$. Since the relaxation times in the BGK and Fokker–Planck models are free to be chosen at this time, they can be fixed by $\tau_{\mathrm{BGK}} = \tau_{\mathrm{Boltz}}$ and $\tau_{\mathrm{FP}} = 2\tau_{\mathrm{Boltz}}$. With this choice P_{ij} exhibits the same proportionality factor for all models. However, the factor for P_i differs. This leads to different Prandtl numbers for the different models.

2.3. Consistency with fluid dynamics

The consistency of kinetic models with fluid dynamics have been extensively studied, e.g., in the text books [6,27]. For the case of Fokker–Planck see also [10].

The transfer equations for $\boldsymbol{\Psi}_{\mathrm{cons}}$ yield the conservation laws for mass, momentum and energy, i.e.

$$\frac{\partial \rho}{\partial t} + \frac{\partial \rho U_j}{\partial x_j} = 0, \tag{13}$$

$$\frac{\partial \rho U_i}{\partial t} + \frac{\partial \rho U_i U_j}{\partial x_j} + \frac{\partial p_{ij}}{\partial x_j} = \rho F_i, \tag{14}$$

$$\frac{\partial \rho e_s}{\partial t} + \frac{\partial \rho U_j e_s}{\partial x_j} + \frac{\partial q_j}{\partial x_j} + p_{jk}\frac{\partial U_j}{\partial x_k} = 0. \tag{15}$$

Eqs. (13)–(15) do not depend on the details of the collision model due to the conservation property (5). Hence, all reasonable kinetic models will reproduce the same conservation laws of continuum physics.

The conservation laws form the field equations for $\rho(\boldsymbol{x}, t)$, $\boldsymbol{U}(\boldsymbol{x}, t)$ and $e_s(\boldsymbol{x}, t)$. However, Eqs. (14) and (15) are unclosed due to the appearance of the unknown molecular stress p_{ij} and heat flux q_j. Regarding the molecular stress p_{ij}, the closure problem can be reformulated by splitting p_{ij} into an isotropic part $p\delta_{ij}$ and a deviatoric part π_{ij}, i.e. $p_{ij} = p\delta_{ij} + \pi_{ij}$, where $p = p_{ii}/3$. Comparison with the sensible energy $e_s = 0.5 p_{ii}/\rho$ leads to

$$p = \frac{2}{3}\rho e_s. \tag{16}$$

For perfect gases we are familiar with the equation of state $p = (\gamma - 1)\rho e_s$, where γ is the ratio of specific heats. Eq. (16) reveals that $\gamma = 5/3$, which is in agreement with the known value for monatomic gases. Eq. (16) can also be written according

to the thermal equation of state, i.e. $p = \rho RT$. Here, $R = k/m$ refers to the specific gas constant, which is assumed to be given. Comparison of $p = \rho RT$ with Eq. (16) shows that the sensible energy e_s is related to the temperature T as

$$e_s = \frac{3}{2}RT = \frac{3}{2}\frac{k}{m}T. \tag{17}$$

It remains to specify a closure for the deviatoric stress π_{ij} and the heat flux q_i. We derive transfer equations for these quantities from Eq. (4) by multiplying with $u_{\langle i}u_{j\rangle}$ (deviatoric part of the tensor u_iu_j) and $\frac{1}{2}u_iu_ku_k$, respectively, and integrating over the velocity space. This yields

$$\frac{\partial \pi_{ij}}{\partial t} + \frac{\partial \pi_{ij}U_k}{\partial x_k} + \frac{\partial m_{ijk}}{\partial x_k} + \frac{4}{5}\frac{\partial q_{\langle i}}{\partial x_{j\rangle}} + 2p\frac{\partial U_{\langle i}}{\partial x_{j\rangle}} + 2\pi_{k\langle i}\frac{\partial U_{j\rangle}}{\partial x_k} = P_{ij} \tag{18}$$

for the stress deviator π_{ij} and

$$\frac{\partial q_i}{\partial t} + \frac{\partial q_iU_k}{\partial x_k} + \frac{1}{2}\frac{\partial R_{ik}}{\partial x_k} + p\frac{\partial(\pi_{ik}/\rho)}{\partial x_k} + \frac{5}{2}\frac{k}{m}p_{ik}\frac{\partial T}{\partial x_k} - \frac{\pi_{ij}}{\varrho}\frac{\partial \pi_{jk}}{\partial x_k} + \left(m_{ijk} + \frac{6}{5}q_{\langle i}\delta_{jk\rangle} + q_k\delta_{ij}\right)\frac{\partial U_j}{\partial x_k} = P_i \tag{19}$$

for the heat flux q_i. Note, that the left hand sides of these equations are the same for all kinetic models independent of the collision model. The collision model enters through P_{ij} and P_i. Following the expressions (12), we write

$$P_{ij} = -\frac{1}{\hat{\tau}}\pi_{ij} \quad \text{and} \quad P_i = -\lambda\frac{1}{\hat{\tau}}q_i, \tag{20}$$

where the relaxation times $\hat{\tau}$ and the factor λ have different values for the different models. We have $\hat{\tau} \in \{(\alpha\rho/m)^{-1}, \tau_{\mathrm{BGK}}, \tau_{\mathrm{FP}}/2\}$ and $\lambda \in \{2/3, 1, 3/2\}$ for Boltzmann, BGK and Fokker–Planck, respectively. Still, Eqs. (18) and (19) are not closed, instead, higher order moments of the distribution function occur, namely m_{ijk} and R_{ij}. These have been defined in a convenient way we will not discuss,[1] but only state that these quantities vanish in equilibrium, see e.g. [27]. We emphasize that the closures for π_{ij} and q_i are essentially the same for all collision models given above, except for different values of $\hat{\tau}$, λ and possibly different evolutions for m_{ijk} and R_{ij} by higher moment equations.

The equations for stress (18) and heat flux (19) are typically reduced by an asymptotic expansion, [6,27]. We assume that in a suitable dimensionless formulation the relaxation time $\hat{\tau}$ is small ($\hat{\tau} \ll 1$) and write

$$\pi_{ij} = \pi_{ij}^{(0)} + \hat{\tau}\pi_{ij}^{(1)} + \mathcal{O}(\hat{\tau}^2), \quad q_{ij} = q_{ij}^{(0)} + \hat{\tau}\, q_{ij}^{(1)} + \mathcal{O}(\hat{\tau}^2) \tag{21}$$

while the equilibrium variables ρ, U_i and T remain non-expanded. This corresponds to a Chapman–Enskog expansion of the moment equations. Inserting this expansion into the evolution equations and sorting the powers in $\hat{\tau}$, we immediately find $\pi_{ij}^{(0)} = 0$ and $q_i^{(0)} = 0$ as equilibrium values. For the next expansion coefficient we use $m_{ijk} = \hat{\tau}\, m_{ijk}^{(1)} + \mathcal{O}(\hat{\tau}^2)$ and $R_{ij} = \hat{\tau}\, R_{ij}^{(1)} + \mathcal{O}(\hat{\tau}^2)$, since their equilibrium values vanish. More details on Chapman–Enskog expansions can be found in the literature [6,27]. Ultimately, we find

$$\pi_{ij} = -2\hat{\tau}pS_{ij}^d + \mathcal{O}(\tau^2) \quad \text{and} \tag{22}$$

$$q_i = -\frac{5}{2}\lambda\frac{k}{m}\hat{\tau}p\frac{\partial T}{\partial x_i} + \mathcal{O}(\tau^2) \tag{23}$$

with

$$S_{ij}^d = \frac{1}{2}\left(\frac{\partial U_i}{\partial x_j} + \frac{\partial U_j}{\partial x_i}\right) - \frac{1}{3}\frac{\partial U_n}{\partial x_n}\delta_{ij} \tag{24}$$

for stress and heat flux and can identify the viscosity coefficient μ and the heat conductivity κ as

$$\mu = \hat{\tau}p, \quad \text{and} \quad \kappa = \frac{5k}{2m}\frac{1}{\lambda}\hat{\tau}p. \tag{25}$$

This result shows that all collision models above recover the classical fluid dynamical laws of Navier–Stokes (22) and Fourier (23) in the case of small relaxation times τ. Among the models, differences to Boltzmann occur for the heat conductivity, which results in different Prandtl numbers

$$\mathrm{Pr} := \frac{c_p\mu}{\kappa} = \frac{\frac{5k}{2m}\hat{\tau}p}{\frac{5k}{2m}\frac{1}{\lambda}\hat{\tau}p} = \lambda \tag{26}$$

and hence, for the different models

[1] $m_{ijk} = \int_{\mathbb{R}^3} u_iu_ju_k\mathcal{F}d\boldsymbol{V}$,
$R_{ij} = \int_{\mathbb{R}^3} u_iu_ju_ku_k\mathcal{F}d\boldsymbol{V} - \frac{k}{m}T(7\ \pi_{ij} + 5p\delta_{ij})$.

$$\mathrm{Pr}^{(\mathrm{Boltz})} = \frac{2}{3}, \quad \mathrm{Pr}^{(\mathrm{BGK})} = 1 \quad \text{and} \quad \mathrm{Pr}^{(\mathrm{FP})} = \frac{3}{2}. \tag{27}$$

For most gases, measurements show a more or less constant Prandtl number with a value of 2/3, such that the Boltzmann collision operator gives the best approximation. A possible Prandtl number correction for the Fokker–Planck model can be found in [10].

We conclude, that the Fokker–Planck equation (4) with Eq. (10) can be considered as a valid model for non-equilibrium gases. Especially when the relaxation time is small against the observation time, the Fokker–Planck solution can be expected to give almost perfect agreement with classical fluid dynamics. Therefore, in this paper we will focus on the Fokker–Planck model, which will be useful beyond the validity of classical fluid dynamics.

2.4. Stochastic approximation

For the remainder of the paper we will focus on the Fokker–Planck model and write from now on $\tau_{\mathrm{FP}} \equiv \tau$. In this paper, the Fokker–Planck equation (4) with Eq. (10) is solved through the stochastic motion

$$\frac{dX_i}{dt} = M_i \quad \text{with} \tag{28}$$

$$\frac{dM_i}{dt} = -\frac{1}{\tau}(M_i - U_i) + \left(\frac{4e_s}{3\tau}\right)^{1/2} \frac{dW_i(t)}{dt} + F_i \tag{29}$$

of notional particles, each having a position $\boldsymbol{X}$ and a (molecular) velocity $\boldsymbol{M}$. Note that the notional particles interact, since the mean molecular velocity $\boldsymbol{U}$ and the sensible energy e_s, which appear in Eq. (29), represent statistical moments of the particle ensemble at the particle location $\boldsymbol{X}$ at time t. The mean velocity $\boldsymbol{U}$ is equivalent to the fluid velocity measured on the macroscopic fluid dynamic scale according to the ergodic theorem [9]. The force $\boldsymbol{F}$ in Eq. (29) represents the external force in Eq. (4). According to Eq. (29), the particle velocity is driven by a drift towards the macroscopic gas velocity and a stochastic noise term governed by the derivative of a Wiener process $\boldsymbol{W}(t)$. A Wiener process is a Gaussian process with $dW_i(t) = W_i(t+dt) - W_i(t)$, $\langle dW_i(t)\rangle \equiv 0$ and $\langle dW_i(t) dW_j(t)\rangle \equiv dt\delta_{ij}$. It is important that the loss of sensible energy due to the drift term is statistically always exactly matched by the gain of e_s due to the diffusion term. The correlation time scale τ represents the relaxation time of the Fokker–Planck equation. In comparison with the Boltzmann equation, the appearance of the first and second right hand side terms in (29) can be seen as the integral effect of molecular interactions, which produce a continuous sequence of small and almost stochastic velocity changes.

In the limit of infinite particle paths $\{\boldsymbol{X}^{(\alpha)}, \boldsymbol{M}^{(\alpha)}\}_{\alpha\in\mathbb{N}}$ (α is the particle index) simulated according to Eqs. (28) and (29), the distribution function of the velocities $\boldsymbol{M}^{(\alpha)}$ at a space point $\mathbf{x}$ converges to the solution $\mathcal{F}(\boldsymbol{V}, \boldsymbol{x}, t)$ of the Fokker–Planck equation (4) with (10); $\boldsymbol{V}$ is the independent velocity sample space variable. Note, that the particle paths are coupled through the averaged quantities $\boldsymbol{U}$ and e_s.

The stochastic model, i.e. Eqs. (28) and (29), and the implied Eqs. (18) and (19) for the stress tensor $\pi_{ij}(\mathbf{x}, t)$ and heat flux $q_i(\mathbf{x}, t)$ are unclosed as long as the characteristic time scale $\tau = \hat{\tau}$ is not defined. In Eq. (25), the relaxation time $\hat{\tau}$ (note that here $\hat{\tau} = \tau_{\mathrm{FP}}/2$ and for simplicity we write $\tau = \tau_{\mathrm{FP}}$) was related to the viscosity of the gas μ by

$$\mu = \frac{\tau p}{2}. \tag{30}$$

For gases, μ depends only on temperature with a power law of the form

$$\mu = \mu_0 \left(\frac{T}{T_0}\right)^{\omega} \tag{31}$$

with reference temperature T_0, reference viscosity μ_0 and viscosity exponent $1/2 \leqslant \omega \leqslant 1$. The two extreme values are given for the case of a gas of hard spheres ($\omega = 1/2$) or Maxwell molecules ($\omega = 1$). For realistic gases one finds $\omega \approx 0.7$—0.8. The formula (31) is now used to find an explicit expression for τ, i.e.

$$\tau = 2\frac{\mu_0}{p}\left(\frac{T}{T_0}\right)^{\omega} = \tau_0 \frac{\rho_0}{\rho}\left(\frac{T}{T_0}\right)^{\omega-1}. \tag{32}$$

The scales T_0 and τ_0 can be determined in the following way. We assume that a characteristic reference length L_0, reference velocity U_0, Reynolds number Re and Mach number Ma are given for a flow considered. By introducing the speed of sound $a_0 = (\gamma R T_0)^{1/2}$, the Mach number $Ma = U_0/a_0$ can be written as

$$Ma = \frac{U_0}{\sqrt{\gamma R T_0}} \tag{33}$$

and similarly, for the Reynolds number $Re = U_0 L_0 \rho_0/\mu_0$, one finds

$$Re = \gamma \frac{L_0}{U_0 \tau_0} Ma^2. \tag{34}$$

Thus, the knowledge of $L_0,\ U_0,\ Re$ and Ma enables the calculation of $e_0 = 3RT_0/2$ and τ_0 via Eqs. (33) and (34).

The inverse relaxation time τ^{-1} corresponds to the mean collision frequency of the gas particles and, hence, gives rise to a mean free path $\lambda_0 = a_0\tau_0$. The Knudsen number λ_0/L_0 is the essential scaling parameter in non-equilibrium gases and satisfies the following relations

$$Kn = \frac{1}{Ma}\frac{\tau_0}{t_0} = \gamma \frac{Ma}{Re} \tag{35}$$

with a reference observation time $t_0 = L_0/U_0$.

3. Discussion of the model

In this section, the relation of the proposed model to several existing approaches to replace the Boltzmann equation by simpler stochastic equations are discussed.

3.1. Range of applicability

The Fokker–Planck equation or its stochastic Langevin formulation has been first investigated as a model for molecules by Kirkwood [14]. Major assumption for this model is a dense state of the molecules interacting on a fast time scale which allows for a stochastic description of the particle dynamics on microscopic scales. This is typically the case for liquids. Similarly, Cercignani [6] derived the Fokker–Planck operator in the limit of an infinite cross section for the particle interaction which represents a dense gas. Hence, it is necessary to further explain why this paper proposes to use Fokker–Planck as a model for rarefied gases with larger Knudsen numbers.

While there is not yet a formal mathematical statement about the approximation quality of the Fokker–Planck (10) operator with respect to the Boltzmann operator (7) we base our argument on a number of observations and investigations.

- As shown for example in [17] the velocity distribution function for the Fokker–Planck equation matches well with the Boltzmann distribution for small Knudsen numbers $Kn \to 0$, i.e., close to equilibrium. Some deviations can be adjusted by choosing the proper relaxation time τ_{FP}, but differences remain for example in the value of the Prandtl number. This indicates that Fokker–Planck is a valid approximation for small Knudsen numbers. On the other hand in the case of large relaxation times, i.e., $Kn \to \infty$, both the Fokker–Planck and Boltzmann equation reduce formally to the collision-less free flight equation. This suggests that flows with very large Knudsen numbers could also be described by a Fokker–Planck equation.
- The moments obtained from the Fokker–Planck collision operator show a strong resemblance to the moments of the Boltzmann collision integral. For the second and third moment, this has been demonstrated in the above sections. A detailed investigation unveils that also higher moments exhibit a linear relaxational form with respect to the corresponding moment of the velocity distribution. This is identical to the linearized Boltzmann operator and the BGK model. Additionally, the relaxation time of a particular moment is always proportional to the fundamental relaxation time τ of the respective model. Assuming that similar behavior of the moments means a similar behavior of the collision operators, Fokker–Planck can be considered as an approximation to at least linearized Boltzmann or BGK.
- Numerically the solution algorithm strongly resembles the direct simulation Monte-Carlo (DSMC) method. Essentially the detailed random calculation of new particle velocities is replaced by a random disturbance based on the respective state of the gas. This could be viewed as a special molecular interaction.

Altogether, we conclude that the range of Knudsen numbers where the Fokker–Planck model can be applied needs an extensive investigation, both theoretically and computationally. Our current justification is essentially based on a mathematical comparison with the Boltzmann equation. To some extend we use the Fokker–Planck operator purely as a mathematical or computational tool to approximate Boltzmann equation. First indications for the success of this approach are demonstrated in computational experiments below.

3.2. Relation to stochastic particle methods

One way is to assume that the position of a particle represents a stochastic diffusion process [3]. However, this assumption is only valid for time steps that are large compared to a characteristic time scale for molecular velocity correlations, which means one applies a relatively crude model [9]. Hence, this approach has several shortcomings. Macroscopic transport coefficients are not calculated from the molecular dynamics but they have to be introduced as external variables. Furthermore, due to the fact that the dynamics of velocity fluctuations is only asymptotically described, this analysis has to be limited to incompressible flows, i.e. corrections to the Navier–Stokes model cannot be obtained.

A better way to develop stochastic models for the molecular motion is to assume that position and velocity of a particle represent a stochastic diffusion process similar to the one described by Eqs. (28) and (29), which was pioneered by Kirkwood [14,15,33,32,17]. Compared to molecular position models, the consideration of a velocity model has the significant advantage that macroscopic transport coefficients may be obtained as a consequence. Nevertheless, there have been a couple of relevant questions related to the previous use of this approach. First, Kirkwood [14] introduced such a molecular velocity model as a heuristic model for liquids. In this paper, we start with the Fokker–Planck equation as a simplified model derived from the Boltzmann equation. On the kinetic level it is possible to rigorously compare the stochastic model with the description of the Boltzmann equation as shown above. Another question is that Kirkwood's model was applied previously only to recover the Navier–Stokes model. We have argued that the Fokker–Planck operator can be related to the BGK equation and as such represents an approximation to Boltzmann's equation that goes clearly beyond the validity of the Navier–Stokes system. For the success of the BGK model see for example [20].

A more general explanation of molecular motion by stochastic models was presented recently by Heinz [9–11]. The approach applied resulted in a stochastic acceleration model which generalizes Kirkwood's stochastic velocity model. It allows to modify the Prandtl number whose wrong prediction is one of the major drawbacks of the standard velocity model. The combination of the algorithm of the present paper with this advanced model is left for future work.

3.3. Comparison to BGK, Lattice Boltzmann and DSMC

BGK: In many cases numerical simulations of the Boltzmann equation are based on the BGK model introduced above, for example in [20]. Typically, this still requires to discretize the full three-dimensional velocity space in each grid point to accommodate the unknown values of the distribution function. The BGK model however significantly simplifies the collision process. Due to the replacement of the Boltzmann collision operator the BGK equation will only give approximate results.

The new model presented in this paper is similar to BGK in the sense that it replaces the Boltzmann collision operator by a simpler model, namely Fokker–Planck, but due to the implementation as particle method no discretization of the distribution function is necessary. The computational complexity of the new method can be compared to BGK when comparing the number of discretization points for the distribution function in one cell to the average number of particles per cell. While BGK easily requires $10^2 - 10^3$ discretization points the method of this paper uses as few as 10 particles per cell. However, when solving BGK, the statistical noise is completely avoided.

Lattice Boltzmann: Many simulations in fluid dynamics are based on the lattice Boltzmann method, for details see for example the text books [29,31]. In this approach the distribution function is discretized in each space point as well, but with typically few points, which are strongly linked to the space grid allowing for high efficiency. In general, this limits the flexibility of the distribution function significantly and restricts the applicability to close to isothermal and equilibrium processes. This limitation is not given for the current Fokker–Planck model, which at the same time will also be more expensive than lattice Boltzmann.

Direct Simulation Monte-Carlo: The full Boltzmann equation is often solved by a stochastic particle method (DSMC) described by Bird in [5]. It computes the pathes of reference particles similar to the approach of this paper. The macroscopic fields are computed from particle averages as well. However, collisions are modeled directly as binary interaction of the particles in each grid cell. The number of collisions are computed from macroscopic relations for the collision frequency and the collision mechanics follows the Boltzmann collision operator with an appropriate interaction potential.

The current method can be viewed as a modification of DSMC by reducing the binary interaction of the particles to stochastic noise each particle experiences on its path. On the kinetic level this is equivalent to replacing Boltzmann with Fokker–Planck. It increases the efficiency and simplifies the implementation, parallelization, etc. however, at the expense of physical accuracy. Using the advanced numerical algorithm presented below, the new model also allows for larger time steps independent from the resolution of the collisions. Issues with stochastic noise will be the same for the new model and DSMC. Similarly, difficulties due to noise for low Mach number flows can be expected for both methods.

4. Solution algorithm

Here, the numerical solution of Eqs. (28) and (29) is considered, i.e. an algorithm is presented to accurately solve the system

$$\frac{dX_i}{dt} = M_i, \tag{36}$$

$$\frac{dM_i}{dt} = -\frac{1}{\tau}(M_i - U_i) + \left(\frac{4e_s}{3\tau}\right)^{1/2} \frac{dW_i(t)}{dt} + F_i \tag{37}$$

for each member of a large set of computational particles (here $\tau = \tau^{(FP)}$). All these particles have an individual weight w, a position $\boldsymbol{X}$ and a velocity $\boldsymbol{M}$. For simplicity, $w \equiv 1$ for the rest of this paper. Note that the weighted particle cloud density represents the mass density function $\mathcal{F}(\boldsymbol{V}, \boldsymbol{x}, t) = \rho f(\boldsymbol{V}; \boldsymbol{x}, t)$, where $f(\boldsymbol{V}; \boldsymbol{x}, t)$ is the probability density function (PDF) of molecule velocity at location $\boldsymbol{x}$ and time t. As explained earlier, the independent variables V_i represent the sample space

coordinates of the stochastic variables M_i and the consistent evolution of $\mathcal{F}$ in the $\boldsymbol{x}-\boldsymbol{V}$-space is described by the Fokker–Planck equation

$$\frac{\partial \mathcal{F}}{\partial t}+V_i\frac{\partial \mathcal{F}}{\partial x_i}+\frac{\partial}{\partial V_i}\left\{\left[F_i-\frac{1}{\tau}(V_i-U_i)\right]\mathcal{F}\right\}=\frac{\partial^2}{\partial V_i\partial V_i}\left\{\frac{2e_s}{3\tau}\mathcal{F}\right\}. \tag{38}$$

However, due to the high dimensionality of the space in which $\mathcal{F}$ is defined, it is in general unpractical to solve above equation with a deterministic continuum approach and therefore particle Monte Carlo methods are preferred. Their computational cost scales linearly with the sample space dimension and it is an important property for the efficiency of the presented modeling approach that no individual particle collisions like in other methods have to be considered. The particle coupling is solely due to the statistical moments $\boldsymbol{U}$ and e_s, which appear in the evolution equations. These moments can be estimated at the nodes of an imposed computational grid, from where they have to be interpolated to the particle positions. For simplicity, but without loss of generality, here the time scale τ is assumed to be constant. The solution algorithm can be outlined as follows: after imposing an appropriate computational grid and after consistent initialization of the particles, n_t time steps are performed, in each of which

(1) $\boldsymbol{U}$ and e_s at time t are estimated at each grid node and interpolated to the particle positions,
(2) the time step size Δt is determined,
(3) a first half-step is performed to estimate the particle mid-points,
(4) mid-point boundary conditions are applied,
(5) $\boldsymbol{U}$ and e_s at time $t+\Delta t/2$ are interpolated from the grid nodes to the particle mid-point positions,
(6) the new particle velocities and positions are computed and
(7) the boundary conditions are enforced.

Note that in statistical steady state $\boldsymbol{U}$ and e_s do not depend on the time, i.e. $\boldsymbol{U}(t+\Delta t/2)=\boldsymbol{U}(t)$ and $e_s(t+\Delta t/2)=e_s(t)$, but if time accurate simulations are of interest, then the above steps 1–7 may need to be performed multiple times to obtain an accurate estimate of $\boldsymbol{U}(t+\Delta t/2)$ and $e_s(t+\Delta t/2)$ at the mid-points. In the following subsections, the individual components of the algorithm are explained in detail.

4.1. Estimation of statistical moments

To estimate $\boldsymbol{U}$ and e_s at the positions of all particles $j\in\{1,\dots,N_p\}$, first the weighted ensemble averages

$$\boldsymbol{U}(\boldsymbol{x}^J,t)=\frac{\sum_{j=1}^{N_p}\left\{\hat{g}^J(\boldsymbol{X}^j(t))\boldsymbol{M}^j(t)\right\}}{\sum_{j=1}^{N_p}\left\{\hat{g}^J(\boldsymbol{X}^j(t))\right\}}, \tag{39}$$

and

$$e(\boldsymbol{x}^J,t)=\frac{1}{2}\left(\frac{\sum_{j=1}^{N_p}\left\{\hat{g}^J(\boldsymbol{X}^j(t))\boldsymbol{M}^j(t)\cdot\boldsymbol{M}^j(t)\right\}}{\sum_{j=1}^{N_p}\left\{\hat{g}^J(\boldsymbol{X}^j(t))\right\}}-\boldsymbol{U}(\boldsymbol{x}^J,t)\cdot\boldsymbol{U}(\boldsymbol{x}^J,t)\right) \tag{40}$$

are computed for each grid node $J\in\{1,\dots,N_n\}$. Therefore, the kernel functions $\hat{g}^J(\boldsymbol{x})$ with the property

$$\sum_{J=1}^{N_n}\hat{g}^J(\boldsymbol{x})\ \equiv\ 1\quad\forall\boldsymbol{x}\in\Omega \tag{41}$$

are employed. The same kernel functions are also used to interpolate the statistical moments from the grid nodes to the particle positions $\boldsymbol{X}^j(t)$, i.e.

$$\boldsymbol{U}(\boldsymbol{X}^j(t),t)=\sum_{J=1}^{N_n}\left\{\hat{g}^J(\boldsymbol{X}^j(t))\boldsymbol{U}(\boldsymbol{x}^J,t)\right\} \tag{42}$$

and

$$e_s(\boldsymbol{X}^j(t),t)=\sum_{J=1}^{N_n}\left\{\hat{g}^J(\boldsymbol{X}^j(t))e_s(\boldsymbol{x}^J,t)\right\}. \tag{43}$$

Various kernel functions $\hat{g}^J(\boldsymbol{x})$ may be considered, e.g. classical hat functions with $\hat{g}^J(\boldsymbol{x}_I)=\delta_{JI}$, where $\boldsymbol{x}^I$ is the location of grid node I. Since the statistical error of $\boldsymbol{U}$ and e_s reduces only with one over the square root of the number of particles per grid cell, large particle numbers are required. If one is only interested in statistically stationary solutions, however, it is possible to dramatically reduce the required particle number by applying exponentially weighted moving time averaging [13]. Instead of evaluating $\boldsymbol{U}(\boldsymbol{x}^J,t)$ and $e_s(\boldsymbol{x}^J,t)$ at time t according to Eqs. (39) and (40), these moments are calculated as

$$\boldsymbol{U}(\boldsymbol{x}^j,t)=\frac{\mathcal{U}^j(t)}{\mathcal{W}^j(t)} \tag{44}$$

and

$$\boldsymbol{e}_s(\boldsymbol{x}^j,t)=\frac{1}{2}\left(\frac{\mathcal{E}^j(t)}{\mathcal{W}^j(t)}-\boldsymbol{U}^j(t)\cdot\boldsymbol{U}^j(t)\right). \tag{45}$$

The time averaged quantities $\mathcal{U}^j(t)$, $\mathcal{E}^j(t)$ and $\mathcal{W}^j(t)$ are obtained by the expressions

$$\mathcal{U}^j(t)=\mu\mathcal{U}^j(t-\Delta t)+(1-\mu)\sum_{j=1}^{N_p}\left\{\hat{g}^j(\boldsymbol{X}^j(t))\boldsymbol{M}^j(t)\right\}, \tag{46}$$

$$\mathcal{E}^j(t)=\mu\mathcal{E}^j(t-\Delta t)+(1-\mu)\sum_{j=1}^{N_p}\left\{\hat{g}^j(\boldsymbol{X}^j(t))\boldsymbol{M}^j(t)\cdot\boldsymbol{M}^j(t)\right\}\quad\text{and} \tag{47}$$

$$\mathcal{W}^j(t)=\mu\mathcal{W}^j(t-\Delta t)+(1-\mu)\sum_{j=1}^{N_p}\left\{\hat{g}^j(\boldsymbol{X}^j(t))\right\}, \tag{48}$$

where $\mu\in[0,1]$ is a memory factor and Δt the time step size. Note that for $\mu=0$ the expressions (44) and (45) are identical with (39) and (40), respectively. On the other hand, $\mu=1-1/n_a$ leads to results corresponding to solutions, which were averaged over roughly the past n_a time steps (n_a will be referred to as the time averaging factor). These "averaged" solutions lag temporally behind and if they are employed for the transient phase of the simulation, no time accurate results can be expected. However, for statistically stationary calculations this exponentially moving time averaging technique with large n_a (e.g. $n_a\approx 1000$) proved to be extremely effective in reducing statistical and deterministic bias errors; see e.g. [13,12,25]. All the following schemes and test cases are explained for statistically stationary scenarios, for which this time averaging technique can be applied.

4.2. Particle evolution

To compute velocity and position of a particle at the new time $t+\Delta t$ based on the values at time t, the schemes

$$M_i^{n+1}-M_i^n=-\left(1-e^{-\Delta t/\tau}\right)\left(M_i^n-U_i\right)+\sqrt{\frac{C^2}{B}}\xi_{1,i}+\sqrt{A-\frac{C^2}{B}}\xi_{2,i}+F_i\Delta t \tag{49}$$

and

$$\underbrace{X_i^{n+1}-X_i^n}_{\Delta X_i^{n+1}}=U_i\Delta t+\left(M_i^n-U_i\right)\tau\left(1-e^{-\Delta t/\tau}\right)+\sqrt{B}\xi_{1,i}+\frac{F_i}{2}\Delta t^2 \tag{50}$$

are employed, where the superscripts n and $n+1$ denote values at the old and new times t and $t+\Delta t$, respectively. Δt is the time step size, $\xi_{1,i}$ and $\xi_{2,i}$ are independent, normal distributed random variables, and

$$A=\frac{2e_s}{3}\left(1-e^{-2\Delta t/\tau}\right), \tag{51}$$

$$B=\frac{2e_s\tau^2}{3}\left(\frac{2\Delta t}{\tau}-\left(1-e^{-\Delta t/\tau}\right)\left(3-e^{-\Delta t/\tau}\right)\right)\quad\text{and} \tag{52}$$

$$C=\frac{2e_s\tau}{3}\left(1-e^{-\Delta t/\tau}\right)^2. \tag{53}$$

Note that scheme (50) is used both for the mid-point prediction (then with half the time step $\Delta t/2$ instead of Δt) and the full time step. In other words, in order to increase the spatial accuracy, the particles are first evolved in a first half-step according to Eq. (50) with only half the time step size. Thereby, mean velocity $\boldsymbol{U}$ and the internal energy e_s are determined at the old locations of the particles and for the full time step at the estimated mid-points. It is important that the same random variables ξ_1 and ξ_2 are employed for mid-point and full time step predictions. Note that for $\Delta t\to 0$ the schemes (49) and (50) reduce to

$$\frac{M_i^{n+1}-M_i^n}{\Delta t}=-\frac{1}{\tau}\left(M_i^n-U_i\right)+\left(\frac{4e_s}{3\tau\Delta t}\right)^{1/2}\xi_i+F_i\quad\text{and}\quad\frac{X_i^{n+1}-X_i^n}{\Delta t}=M_i^n$$

respectively, which are simple, but consistent finite-difference discretizations of Eqs. (36) and (37).

4.2.1. Derivation of the scheme

Next, it is shown that the schemes (49) and (50) are statistically exact for constant $\boldsymbol{U}$ and e_s, i.e. we prove that for an infinite number of independent realisations the following properties hold for any time step Δt:

(1) If $F_i = 0$, then mean velocity and internal energy are preserved.
(2) The analytically correct velocity autocorrelation is recovered.
(3) Exact first conditional moments $\langle M_i^{n+1} \big| \boldsymbol{M}^n \rangle$ and $\langle \Delta X_i^{n+1} \big| \boldsymbol{M}^n \rangle$ are predicted.
(4) Exact second conditional moments $\langle M_i^{n+1} M_j^{n+1} \big| \boldsymbol{M}^n \rangle$ and $\langle \Delta X_i^{n+1} \Delta X_j^{n+1} \big| \boldsymbol{M}^n \rangle$ are predicted.
(5) Exact joint conditional moments $\langle \Delta X_i^{n+1} M_j^{n+1} \big| \boldsymbol{M}^n \rangle$ are predicted.

For simplicity, but without loss of generality, $U_i = F_i = 0$ is assumed for the following derivations, i.e. the solution of

$$\frac{dX_i}{dt} = M_i \quad \text{and} \tag{54}$$

$$\frac{dM_i}{dt} = -\frac{1}{\tau} M_i + \left(\frac{4e_s}{3\tau}\right)^{1/2} \frac{dW_i(t)}{dt} \tag{55}$$

is considered. The exact solution of Eq. (54) based on Ito calculus [24] is

$$M_i^{n+1} = M_i^n e^{-\Delta t/\tau} + \sqrt{A}\xi_{M,i}, \tag{56}$$

but to derive the coupled solution of $\boldsymbol{X}^{n+1}$ and $\boldsymbol{M}^{n+1}$ it is convenient to first write the integration of $\boldsymbol{M}$ from t to $t + \Delta t$ as

$$M_i^{n+1} = M_i^n e^{-\Delta t/\tau} + \lim_{N\to\infty} \sum_{k=1}^{N} \xi_{k,i} \left(\frac{4e_s}{3\tau} \frac{\Delta t}{N}\right)^{1/2} e^{-k\Delta t/(N\tau)}, \tag{57}$$

where $\xi_{k,i}$ are independent, normal distributed random variables. Multiplication with M_j^{n+1} and subsequent averaging leads to the conditional expectation

$$\left\langle M_i^{n+1} M_j^{n+1} \middle| \boldsymbol{M}^n \right\rangle = M_i^n M_j^n e^{-2\Delta t/\tau} + \delta_{ij} \lim_{N\to\infty} \sum_{k=1}^{N} \frac{4e_s}{3\tau} \frac{\Delta t}{N} e^{-2k\Delta t/(N\tau)}. \tag{58}$$

Note that all cross products disappear, since $\langle \xi_{k,i}\xi_{h,j} \rangle = \delta_{kh}\delta_{ij}$ and $\langle \xi_{k,i} \rangle = 0$ (δ_{ij} denotes the Kronecker delta). The last expression can now be written as

$$\left\langle M_i^{n+1} M_j^{n+1} \middle| \boldsymbol{M}^n \right\rangle = M_i^n M_j^n e^{-2\Delta t/\tau} + \delta_{ij} \frac{4e_s}{3\tau} \int_0^{\Delta t} e^{-2t/\tau} dt = M_i^n M_j^n e^{-2\Delta t/\tau} + \delta_{ij} \frac{2e_s}{3} \left(1 - e^{-2\Delta t/\tau}\right) \tag{59}$$

and therefore

$$M_i^{n+1} = M_i^n e^{-\Delta t/\tau} + \overbrace{\left(\underbrace{\frac{2e_s}{3}\left(1 - e^{-2\Delta t/\tau}\right)}_{A}\right)^{1/2}}^{S_{M,i}} \xi_{M,i} \tag{60}$$

is a statistically exact integration scheme for the particle velocity $\boldsymbol{M}$. Note that $\xi_{M,i}$ is a further normal distributed random variable. By multiplying Eq. (60) with M_i^{n+1} and subsequent (unconditional) averaging one obtains

$$\langle M_i^{n+1} M_i^{n+1} \rangle = \langle M_i^n M_i^n \rangle e^{-2\Delta t/\tau} + 2e_s\left(1 - e^{-2\Delta t/\tau}\right) = \left(\langle M_i^n M_i^n \rangle - 2e_s\right) e^{-2\Delta t/\tau} + 2e_s, \tag{61}$$

which shows that the scheme (60) preserves the internal energy

$$e_s = \frac{\langle M_i^n M_i^n \rangle}{2} \tag{62}$$

independent of the time step size Δt, which is not the case for a simple finite-difference type integration scheme. Moreover, by multiplying scheme (60) with M_i^n and subsequent (unconditional) averaging one obtains

$$\frac{\langle M_i^{n+1} M_i^n \rangle}{\langle M_i^n M_i^n \rangle} = e^{-\Delta t/\tau}, \tag{63}$$

which is the analytically correct correlation coefficient.

Next, a similar approach is employed to derive an exact particle position scheme. Therefore, the integration of the particle velocity (57) is performed, which leads to the particle position $\boldsymbol{X}$ at the new time $t + \Delta t$, i.e.

$$\Delta X_i^{n+1} = X_i^{n+1} - X_i^n = M_i^n \tau\left(1 - e^{-\Delta t/\tau}\right) + \lim_{N\to\infty} \sum_{k=1}^{N} \xi_{k,i} \left(\frac{4e_s}{3\tau} \frac{\Delta t}{N}\right)^{1/2} \tau\left(1 - e^{-k\Delta t/(N\tau)}\right). \tag{64}$$

After multiplication with ΔX_j^{n+1} one obtains the conditional expectation

$$\left\langle \Delta X_i^{n+1}\Delta X_j^{n+1}\middle|\boldsymbol{M}^n\right\rangle = M_i^n M_j^n \tau^2\left(1-e^{-\Delta t/\tau}\right)^2 + \delta_{ij}\lim_{N\to\infty}\sum_{k=1}^{N}\frac{4e_s}{3\tau}\frac{\Delta t}{N}\tau^2\left(1-e^{-k\Delta t/(N\tau)}\right)^2, \tag{65}$$

which can be written as

$$\begin{aligned}\left\langle \Delta X_i^{n+1}\Delta X_j^{n+1}\middle|\boldsymbol{M}^n\right\rangle &= M_i^n M_j^n \tau^2\left(1-e^{-\Delta t/\tau}\right)^2 + \delta_{ij}\frac{4e_s}{3}\tau\int_0^{\Delta t}\left(1-2e^{-t/\tau}+e^{-2t/\tau}\right)dt\\ &= M_i^n M_j^n \tau^2\left(1-e^{-\Delta t/\tau}\right)^2 + \delta_{ij}\frac{2e_s\tau^2}{3}\left(\frac{2\Delta t}{\tau}-\left(1-e^{-\Delta t/\tau}\right)\left(3-e^{-\Delta t/\tau}\right)\right).\end{aligned} \tag{66}$$

This leads to the integration scheme

$$\Delta X_i^{n+1} = M_i^n\tau\left(1-e^{-\Delta t/\tau}\right) + \overbrace{\left(\underbrace{\frac{2e_s\tau^2}{3}\left(\frac{2\Delta t}{\tau}-\left(1-e^{-\Delta t/\tau}\right)\left(3-e^{-\Delta t/\tau}\right)\right)}_{B}\right)^{1/2}}^{S_{X,i}}\xi_{X,i}, \tag{67}$$

which together with Eq. (60) is exact provided the two normal distributed random variables $\xi_{X,i}$ and $\xi_{M,i}$ are correctly correlated. To achieve this, we now derive the correlation of velocity and dislocation. Therefore we multiply Eq. (57) with Eq. (64) and take the conditional expectation, which leads to

$$\begin{aligned}\left\langle M_i^{n+1}\Delta X_j^{n+1}|\boldsymbol{M}^n\right\rangle &= M_i^n M_j^n\tau\left(e^{-\Delta t/\tau}-e^{-2\Delta t/\tau}\right) + \delta_{ij}\lim_{N\to\infty}\sum_{k=1}^{N}\frac{4e_s}{3\tau}\frac{\Delta t}{N}\tau\left(e^{-k\Delta t/(N\tau)}-e^{-2k\Delta t/(N\tau)}\right)\\ &= M_i^n M_j^n\tau\left(e^{-\Delta t/\tau}-e^{-2\Delta t/\tau}\right) + \delta_{ij}\frac{4e_s}{3}\int_0^{\Delta t}\left(e^{-t/\tau}-e^{-2t/\tau}\right)dt\\ &= M_i^n M_j^n\tau\left(e^{-\Delta t/\tau}-e^{-2\Delta t/\tau}\right) + \delta_{ij}\underbrace{\frac{2e_s\tau}{3}\left(1-e^{-\Delta t/\tau}\right)^2}_{C}.\end{aligned} \tag{68}$$

The remaining task consists in correctly correlating the stochastic terms in Eqs. (60) and (67), such that Eq. (68) is honored. This can be achieved for example by replacing $S_{M,i}$ and $S_{X,i}$ with

$$S'_{M,i} = \left(\frac{C^2}{B}\right)^{1/2}\xi_{1,i} + \left(A-\frac{C^2}{B}\right)^{1/2}\xi_{2,i} \quad \text{and} \tag{69}$$

$$S'_{X,i} = (B)^{1/2}\xi_{1,i}, \tag{70}$$

respectively, where the normal distributed random variables $\xi_{1,i}$ and $\xi_{2,i}$ are independent. Note that

$$\langle S'_{M,i}S'_{M,j}\rangle = \langle S_{M,i}S_{M,j}\rangle = \delta_{ij}A \quad \text{and} \tag{71}$$

$$\langle S'_{X,i}S'_{X,j}\rangle = \langle S_{X,i}S_{X,j}\rangle = \delta_{ij}B, \tag{72}$$

but in addition also

$$\langle S'_{M,i}S'_{X,j}\rangle = C \tag{73}$$

is ensured, which is the correct covariance. It can easily be verified that all terms are real, i.e. $C^2/B \geqslant 0,\ A - C^2/B \geqslant 0$ and $B \geqslant 0$.

With this it has been shown that the combined exact schemes

$$M_i^{n+1} - M_i^n = -\left(1-e^{-\Delta t/\tau}\right)M_i^n + \sqrt{\frac{C^2}{B}}\xi_{1,i} + \sqrt{A-\frac{C^2}{B}}\xi_{2,i} \quad \text{and} \tag{74}$$

$$\Delta X_i^{n+1} = M_i^n\tau\left(1-e^{-\Delta t/\tau}\right) + \sqrt{B}\xi_{1,i} \tag{75}$$

fulfill the properties listed at the beginning of this subsection. Note that Eqs. (49) and (50) represent the generalization of the exact schemes (74) and (75) for $U_i \neq 0 \neq F_i$.

4.2.2. Validation of the scheme

For illustration, next the superiority of the schemes (74) and (75) compared with the commonly used ones

$$M_i^{n+1} - M_i^n = \left[-\frac{\Delta t}{\tau}M_i^n + \left(\frac{4e_s}{3\tau}\Delta t\right)^{1/2}\xi_i\right]\left[1-\frac{\Delta t}{2\tau}\right] \quad \text{and} \tag{76}$$

$$\Delta X_i^{n+1} = \frac{\Delta t}{2}\left(M_i^n + M_i^{n+1}\right) \tag{77}$$

is demonstrated. To keep the statistical error small, 10^5 independent particles were employed in each of the following numerical experiments.

In the first test case, the velocity distribution of the ensemble at $t' = t/\tau = 0$ is multivariate Gaussian and isotropic with $e_s = 1m^2s^{-2}$. Note that e_s in Eqs. (74) and (76) is extracted from the ensemble at the beginning of every time step. Fig. 1(a) shows e_s as a function of time computed with the common schemes (76) and (77) using different time step sizes. Even for the smallest time steps one can observe a significant decay of e_s and the energy loss rate certainly becomes inacceptable for $\Delta t > \tau/16$. On the other hand, with the new exact scheme, no deterministic energy error can be observed (Fig. 1(b)), even for time steps as large as 10τ. With the second test case, the accuracy of conditional ensemble statistics as a function of the time step size is investigated. This time, all particles have the same initial velocity $\boldsymbol{M}(t=0) = (1,0,0)^T m/s$ and e_s is treated as a constant coefficient with a value of $1m^2/s^{-2}$. Figs. 2 and 3 show the first conditional moments $\langle X_1(t)|\boldsymbol{M}(t=0)\rangle$ and $\langle M_1(t)|\boldsymbol{M}(t=0)\rangle$, respectively. The left plots represent results obtained with the common schemes (76) and (77). Both conditional first moments show significant errors for $\Delta t \geqslant \tau/2$ (the solution with $\Delta t = \tau/16$ serves as a reference). With the new

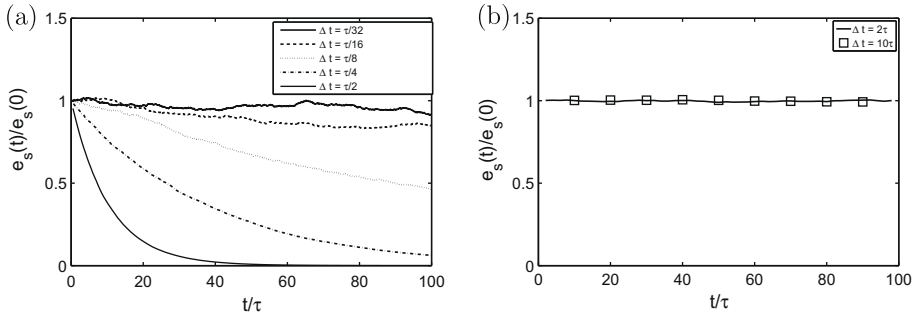

Fig. 1. e_s for $t/\tau \in [0,100]$ with the common scheme (left) and with the new exact scheme (right). For both schemes, different time steps were employed, i.e. $\Delta t \in \{\tau/32, \tau/16, \tau/8, \tau/4, \tau/2\}$ for the common scheme and $\Delta t \in \{2\tau, 10\tau\}$ for the new exact scheme.

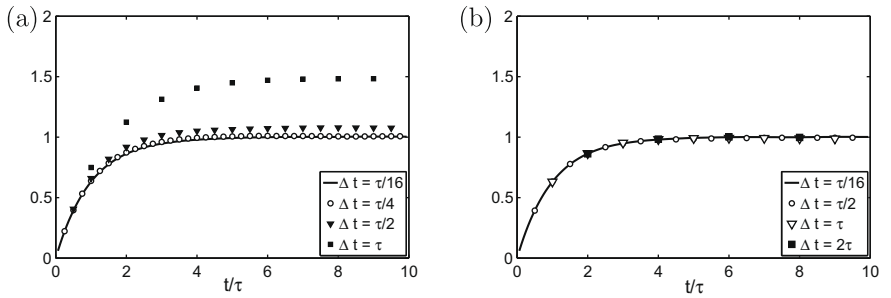

Fig. 2. $\langle X_1|\boldsymbol{M}(t=0)\rangle$ for $t/\tau \in [0,10]$ with the common scheme (left) and with the new exact scheme (right). For both schemes, different time steps were employed, i.e. $\Delta t \in \{\tau/16, \tau/4, \tau/2, \tau\}$ for the common scheme and $\Delta t \in \{\tau/16, \tau/2, \tau, 2\tau\}$ for the new exact scheme.

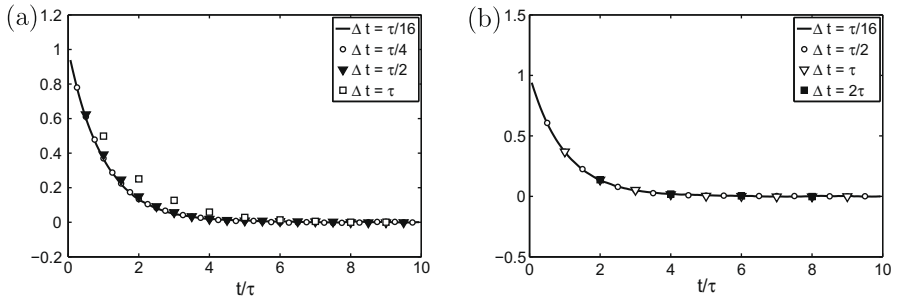

Fig. 3. $\langle M_1|\boldsymbol{M}(t=0)\rangle$ for $t/\tau \in [0,10]$ with the common scheme (left) and with the new exact scheme (right). For both schemes, different time steps were employed, i.e. $\Delta t \in \{\tau/16, \tau/4, \tau/2, \tau\}$ for the common scheme and $\Delta t \in \{\tau/16, \tau/2, \tau, 2\tau\}$ for the new exact scheme.

exact scheme, on the other hand, no deterministic error can be detected (Figs. 2 and 3(b)); even not for $\Delta t = 2\tau$. The same can be stated for the second conditional moments $\langle X_1(t)X_1(t)|\boldsymbol{M}(t=0)\rangle$, $\langle M_1(t)M_1(t)|\boldsymbol{M}(t=0)\rangle$ and $\langle X_1(t)M_1(t)|\boldsymbol{M}(t=0)\rangle$, which are depicted in Figs. 4–6, respectively.

4.3. Boundary conditions

Periodic-, open- and wall-boundary conditions are considered here. In each case, one first has to determine the intersection $\boldsymbol{x}^{inter}$ of the computed particle trajectory with the boundary and the boundary unit normal vector $\boldsymbol{n}$ at $\boldsymbol{x}^{inter}$ pointing out of the domain.

To explain the implementation of periodic boundary conditions, a periodic domain Ω of length $|\boldsymbol{r}|$ in the periodic direction is considered. The corrected position of a particle j, which left the domain across such a boundary, becomes

$$\{\boldsymbol{X}^j\}^{corr} = \begin{cases} \{\boldsymbol{X}^j\}^{actual} - \boldsymbol{r} & \text{if } \boldsymbol{r}\cdot\boldsymbol{n} > 0, \\ \{\boldsymbol{X}^j\}^{actual} + \boldsymbol{r} & \text{else.} \end{cases} \tag{78}$$

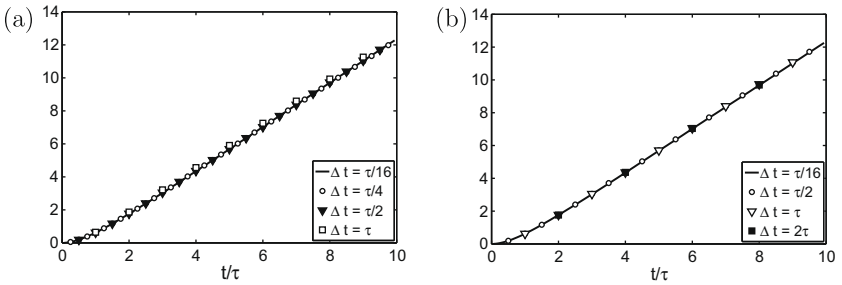

Fig. 4. $\langle X_1X_1|\boldsymbol{M}(t=0)\rangle$ for $t/\tau \in [0,10]$ with the common scheme (left) and with the new exact scheme (right). For both schemes, different time steps were employed, i.e. $\Delta t \in \{\tau/16, \tau/4, \tau/2, \tau\}$ for the common scheme and $\Delta t \in \{\tau/16, \tau/2, \tau, 2\tau\}$ for the new exact scheme.

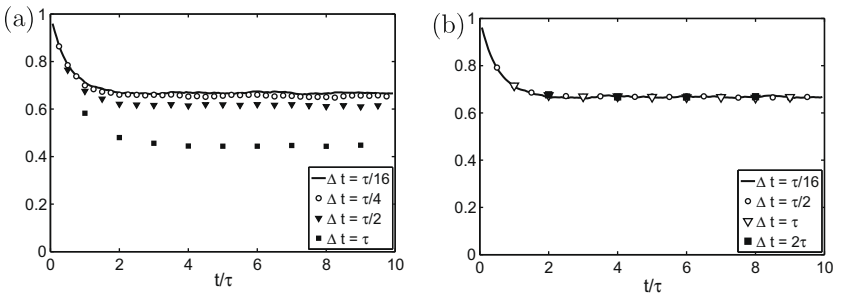

Fig. 5. $\langle M_1M_1|\boldsymbol{M}(t=0)\rangle$ for $t/\tau \in [0,10]$ with the common scheme (left) and with the new exact scheme (right). For both schemes, different time steps were employed, i.e. $\Delta t \in \{\tau/16, \tau/4, \tau/2, \tau\}$ for the common scheme and $\Delta t \in \{\tau/16, \tau/2, \tau, 2\tau\}$ for the new exact scheme.

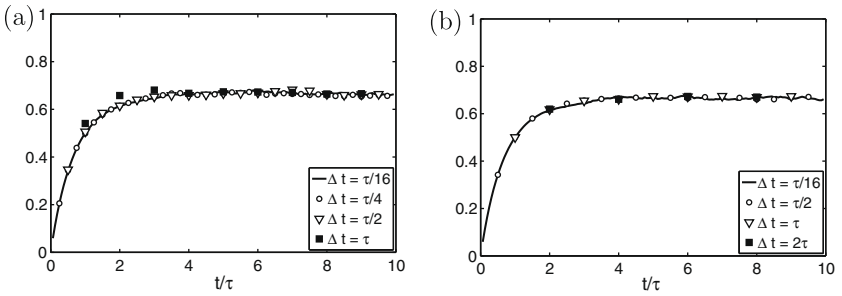

Fig. 6. $\langle X_1M_1|\boldsymbol{M}(t=0)\rangle$ for $t/\tau \in [0,10]$ with the common scheme (left) and with the new exact scheme (right). For both schemes, different time steps were employed, i.e. $\Delta t \in \{\tau/16, \tau/4, \tau/2, \tau\}$ for the common scheme and $\Delta t \in \{\tau/16, \tau/2, \tau, 2\tau\}$ for the new exact scheme.

To treat open boundaries (in- and outflow), buffer regions are introduced, which have to be consistently populated with new particles at the beginning of each time step. Note that mass balance errors might occur, if the buffer region is not wide enough. This problem is avoided, if the more sophisticated in- and outflow boundary condition formulation by Meyer and Jenny [19] is employed. Note that particles which leave the domain Ω through open boundaries are deleted at the end of each time step.

More delicate is the treatment of wall-boundaries. While this is an interesting and challenging topic on its own, we emphasize that no attempt is made here to improve existing approaches. For the studies shown in this paper, isothermal walls are considered and a method which ensures exact mass balance is employed. The wall is treated as an interface between the computational and a virtual domain, in which the marginal distribution of each molecular velocity component is

$$f^{wall} = \frac{1}{(2\pi kT^{wall}/m)^{1/2}} \exp\left(-\frac{V_i^2}{2kT^{wall}/m}\right). \tag{79}$$

The wall-normal velocity distribution of the molecules crossing the wall interface from the virtual into the computational domain is

$$f^{normal} = \frac{-H(-V_n)V_n}{Q} \frac{1}{(2\pi kT^{wall}/m)^{1/2}} \exp\left(-\frac{V_n^2}{2kT^{wall}/m}\right), \tag{80}$$

where $H(\cdot)$ is the Heaviside function and $1/Q$ a normalization factor to ensure that the integration of f^{normal} over the whole V_n-space is identical one. Note that velocities with a negative wall-normal component are directed into the computational domain. The distributions f^{normal} and f^{wall} are depicted in Fig. 7. Now, the treatment of isothermal walls is straight forward: as soon as a computational particle crosses an isothermal wall interface, a new random velocity is assigned to it, where the distributions f^{wall} and f^{normal} are applied for the tangential and normal components, respectively. Location and time of collision with the wall, i.e. $\boldsymbol{x}^{inter}$ and t^{inter}, respectively, are estimated based on linear interpolation. The particle position is then set equal to $\boldsymbol{x}^{inter}$ and a new velocity is assigned as described above. For the remaining part of the time step, i.e. for $\Delta t^{remaining} = t^{n+1} - t^{inter}$, where t^{n+1} is the time at the end of the current time step, the schemes (49) and (50) are applied to compute the new particle position and velocity.

4.4. Comparison to DSMC

DSMC implements the free flight of the particles and the collisions in a fully decoupled way. Over a given time step the particles are moved according to their velocities and in between time steps collisions are simulated with particles staying in place. Typically, the computational domain is covered by a mesh whose cells accommodate a fluctuating number of particles. The particles in each cell are used to obtain averaged values for continuum quantities like density and temperature on the computational mesh. These macroscopic values are also used in determining the characteristics of the particle collisions in each mesh cell. The collisions are conducted pair-wise after selecting two particles per cell at random with a certain acceptance rate. The new velocities are produced according to an interaction model like hard spheres where the scattering angle is again chosen at random or on the basis of a randomized function.

The stochastic algorithm described above also requires macroscopic fields to be computed and updated time-stepwise on a computational mesh. The main differences to DSMC are the treatment of collisions and the coupling of transport and collisions over one time step. Both concepts increase the efficiency of the new method over DSMC. At the same time the new method lacks some of the physical ingredients of DSMC and can be expected to produce less accurate quantitative results.

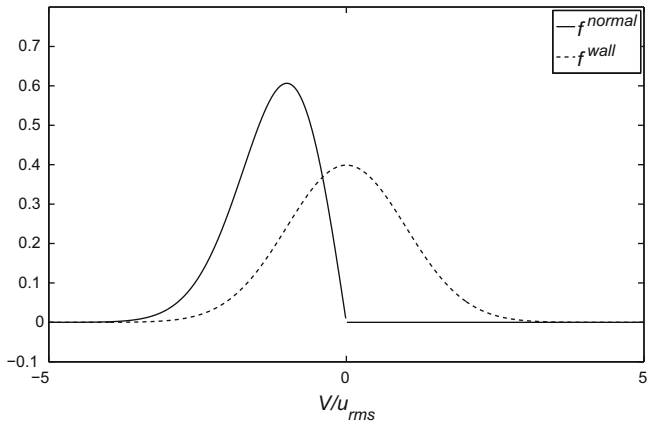

Fig. 7. Marginal PDF's f^{normal} and f^{wall} of the wall-normal and wall-tangential velocity components.

First, the effect of collisions is reduced to stochastic noise on the particle's velocity. This means that the only coupling of the particles is within the averaging to obtain the macroscopic fields. The actual collisions are operations on single particles without complicated pair interaction and scattering calculations. In this way only two (or four, for second order accuracy) random numbers are necessary per particles and time step independent of density and Knudsen number. In DSMC collision-dominated flow regimes close to equilibrium typically slow down the computation. Note that DSMC is reported to have a computational complexity of the order $\mathcal{O}(Kn^{-4})$, see [1]. This problem is overcome with the new method.

Second, the transport step and the collisions are coupled in the new method. This is obvious from the influence of the noise *both* on the velocity and position update, see (49) and (50). The full decoupling of DSMC renders it an essentially first order method. The new method respects changing collision regimes during the flight of a particle within one time step. The coupling also leads to a time step which can be chosen independently from the relaxation time, i.e., Knudsen number. This contributes to the efficient computation especially of collision-dominated regimes.

In the numerical method we chose a time step restricted by a CFL condition such that the particles did not travel beyond their neighboring cells. This is similar to DSMC. However, the coupling of the particle transport and collisions and the decoupling of the collisions between particles allows to design a method with less restrictive CFL condition. In such a scheme particles could move beyond several mesh cells containing frozen macroscopic fields.

5. Numerical experiments

The main objective of the following numerical experiments is to demonstrate the validity of the Fokker–Planck model beyond Navier–Stokes. But also accuracy, generality and efficiency of the stochastic solution algorithm are assessed and the superiority of the new particle time stepping scheme is demonstrated.

5.1. Knudsen paradox

In a first numerical experiment, the ability of the proposed model to correctly predict the Knudsen Paradox is investigated. The Knudsen Paradox has been observed in experiments of channel flow with varying channel width or equivalently different pressures, see [16]. If the normalized mass flux through the channel is plotted over the Knudsen number based on the channel width a distinct minimum is observed around $Kn = 0.8$. This is a paradoxical behaviour because, based on the Navier–Stokes equations, one would expect the mass flux to decrease with increasing the Knudsen number. The minimum can be understood intuitively by considering the two extreme cases of very small and very large Knudsen numbers. For very small Kn the viscosity vanishes and a fully developed steady state channel flow shows infinite flux. On the other hand, the particles stop interacting for large Knudsen numbers. Because of the constant acceleration due to the external force, the steady state again will show infinite flux.

To simulate the Knudsen paradox, we consider Poiseuille flow between two parallel infinite plates at a distance L_0. The driving acceleration $\boldsymbol{F} = (0, 0, F)^T$ is chosen such that the resulting Mach number remains small, i.e. $\rho \approx \rho_0$ and $p \approx p_0$, where ρ_0 and p_0 are reference density and pressure values. The mass flux resulting from the Navier–Stokes equations is

$$J = \frac{F\rho_0^2 L_0^3}{12\mu} \tag{81}$$

and the viscosity $\mu = p_0\tau/2$ gives rise to a mean free path of

$$\lambda = \frac{u_{rms}\tau}{2}, \tag{82}$$

which leads to the Knudsen number

$$Kn = \frac{\lambda}{L_0}. \tag{83}$$

Note that the definition $\lambda = u_{rms}\tau/2$ with $u_{rms} = \sqrt{p_0/\rho_0}$ (rather than $\lambda = a_0\tau$) is used here in order to be consistent with the results presented in [23]. Now, the time scale τ is obtained as a function of $\rho_0,\ p_0,\ L_0$ and the Knudsen number. In addition, we define the dimensionless mass flux

$$\widehat{J} = \frac{J}{\rho_0 u_{rms} L_0} \tag{84}$$

and the dimensionless acceleration

$$\widehat{F} = \frac{F}{u_{rms}^2/L_0}. \tag{85}$$

Fig. 8 shows $\widehat{J}/\widehat{F}$ as a function of the Knudsen number as predicted by the method presented in this paper, by the linearized Boltzmann equation with hard sphere particle interaction [23] and by the Navier–Stokes equation (with no-slip boundary conditions $\widehat{J}/\widehat{F} = 1/(12\ Kn)$). As a reference also the experimental data by Dong [8] is depicted. Note that the linearized Boltzmann equation, which is obtained from Eq. (7) when expanded around a global equilibrium distribution function

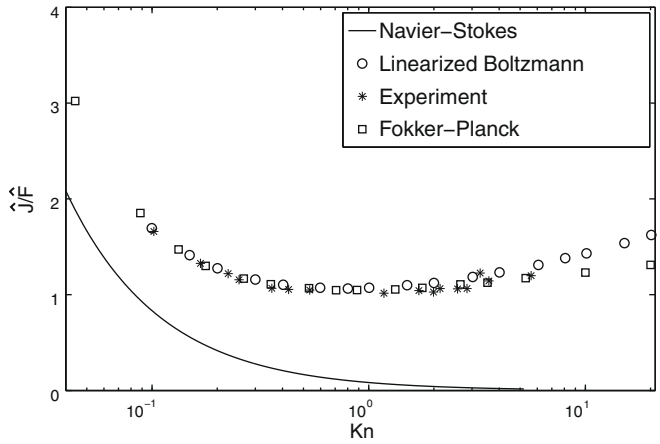

Fig. 8. $\widehat{J}/\widehat{F}$ as a function of the Knudsen number Kn obtained with the linearized Boltzmann model, the Fokker–Planck model and Navier–Stokes.

(for details see also [6]), tends to overpredict the experimental data for $Kn > 1$, while the Fokker–Planck model predictions are in good agreement with the experiments for the measured Knudsen number range from 0.1 to approximately 5. To which extent the discrepancy between the Fokker–Planck and the linearized Boltzmann results are due to the boundary conditions remains to be investigated. It has to be mentioned, however, that the joint PDF of the wall-parallel and wall-normal velocity components can be far from Gaussian at large Knudsen numbers. Fig. 9 shows that this can be represented by the Fokker–Planck model. Shown are the joint PDFs of $M_1^* = M_1/(L_0F/u_{rms})$ and $M_2^* = M_2/(L_0F/u_{rms})$ at $x_1 = 0$ and $x_1 = L_0/2$ obtained for $Kn = 0.044$ and $Kn = 5.3$. While the joint PDF is close to equilibrium (Maxwell distributiuon) for $Kn = 0.044$, it attains a complex shape for $Kn = 5.3$. Interesting is the observation at $x_1 = 0$ (wall), where M_2 conditional on positive M_1-values (molecules moving away from the wall) follows a Maxwell distribution with zero mean. This is not the case for the PDF of M_2 conditional on negative M_1-values (molecules moving towards the wall).

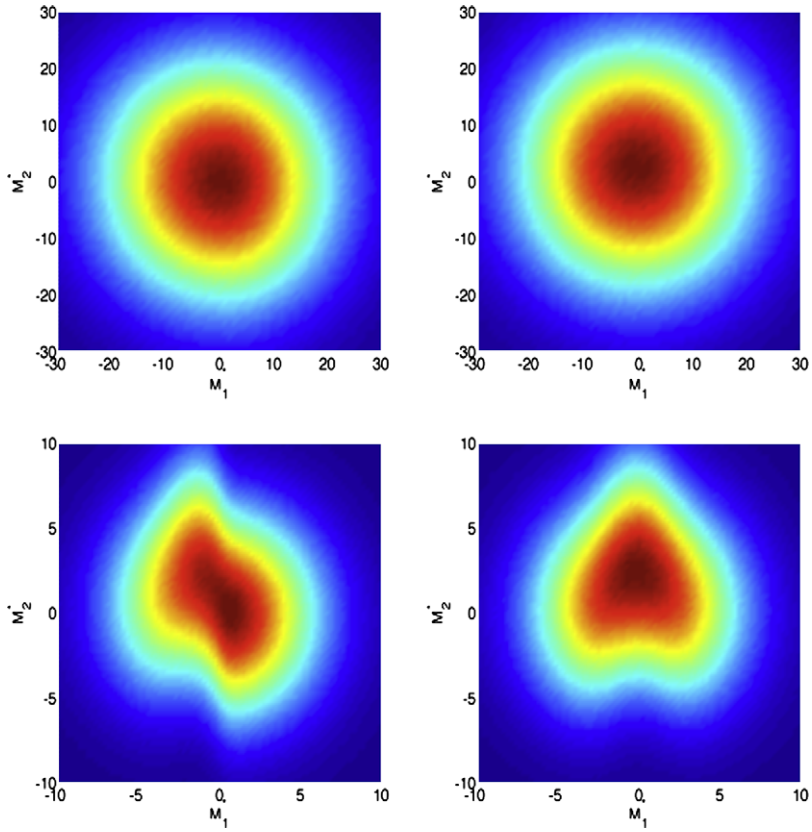

Fig. 9. Joint PDFs of M_1^* and M_2^* at $x_1 = 0$ (left) and $x_1 = L_0/2$ (right) for $Kn = 0.044$ (top) and $Kn = 5.3$ (bottom).

For the own simulations the driving acceleration was adjusted to keep the Mach number

$$Ma = \frac{J}{\rho_0 a_0 L_0} \tag{86}$$

below 0.3. Moreover, a uniformly spaced, Cartesian 2D grid with 32×1 cells and 10 particles per cell (in average) were employed. At the top and bottom of the domain, periodic boundary conditions were applied and at the left and right boundaries isothermal walls were considered. Steady state solutions for Knudsen numbers from 0.04 to 20.0 were computed and to reduce the statistical and bias errors, exponentially weighted time averaging was applied (which has the same effect as increasing the number of particles). The time step size Δt was determined according to a CFL condition as

$$\Delta t = 0.5 \frac{h}{u_{rms}}, \tag{87}$$

where h is the grid spacing. Note that much of the discrepancy between the Navier–Stokes and the other results is due to the slip boundary conditions, which are enforced in the Navier–Stokes simulations, but not for the Fokker–Planck and linearized Boltzmann calculations (there the slip velocity is an outcome of the simulation). How the slip velocity increases with the Knudsen number can observed in Fig. 10, which shows the velocity profiles (normalized with $J\rho_0^{-1}L_0^{-1}$) for $Kn = 0.044$, $Kn = 0.71$ and $Kn = 5.3$ (computed with the Fokker–Planck model). Fig. 11 shows a more detailed comparison between the Fokker–Planck model and DSMC for $Kn = 0.072$. Depicted are the profiles of the normalized quantities $U_2^* = U_2/(L_0F/u_{rms})$, $\pi_{12}^* = \pi_{12}/u_{rms}^2$, $\pi_{22}^* = \pi_{22}/u_{rms}^2$, $T^* = T/T^{wall}$, $q_1^* = q_1/u_{rms}^3$ and $q_2^* = q_2/u_{rms}^3$, where $L_0F/u_{rms}^2 = 0.235$. While velocity and molecular stresses are in excellent agreement, there exist differences in the temperature and heat flux profiles. Such discrepancies have to be expected due to the disagreement of the Prandtl numbers (as discussed earlier). Qualitatively, however, the temperature and heat flux profiles depict the same characteristics. Note for example that Navier–Stokes cannot predict the local temperature minimum in the center of the channel nor the non-zero values of q_2^* and π_{11}^*.

The dependence on grid resolution is shown in Table 1, where the values of $J/J^{converged}$ for $Kn = 5.3$ resulting from simulations with the new method on grids with 64, 32, 16, 8 and 4 cells are shown (here, $J^{converged}$ represents the value obtained for a grid with 64 cells). An asymptotic analysis of the solutions obtained with the finest three grids leads to the conclusion that the spatial discretization error is of at least second order. It is interesting that the solution obtained with a grid consisting of only 4 cells differs from the one with 64 cells by less than 6%. Moreover, for $Kn = 5.3$ with a grid consisting of 32 cells, one simulation with half the time step size and another one with twice the number of particles per cell were performed. The differences between the three values of $\widehat{J}/\widehat{F}$ are of the same order as the statistical error, which confirms that the time step size $\Delta t = 0.5h/u_{rms}$ is small enough. (see Table 2).

5.2. Flow around cylinder

The objective of the second test case is to demonstrate that the proposed algorithm is efficient to compute statistically stationary solutions of flow scenarios involving more complex geometries. Moreover, it is illustrated that there is a significant benefit from the new particle time stepping scheme. We consider a rectangular domain $\Omega = L_0 \times L_0$ with an embedded

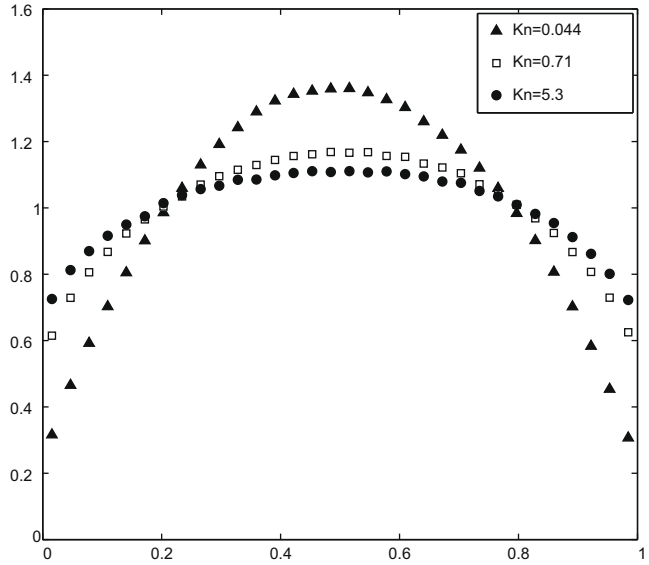

Fig. 10. Velocity profiles normalized with $J\rho_0^{-1}L_0^{-1}$ computed with the new Fokker–Planck model for $Kn = 0.044$, $Kn = 0.71$ and $Kn = 5.3$; x_1 is the distance from the left wall.

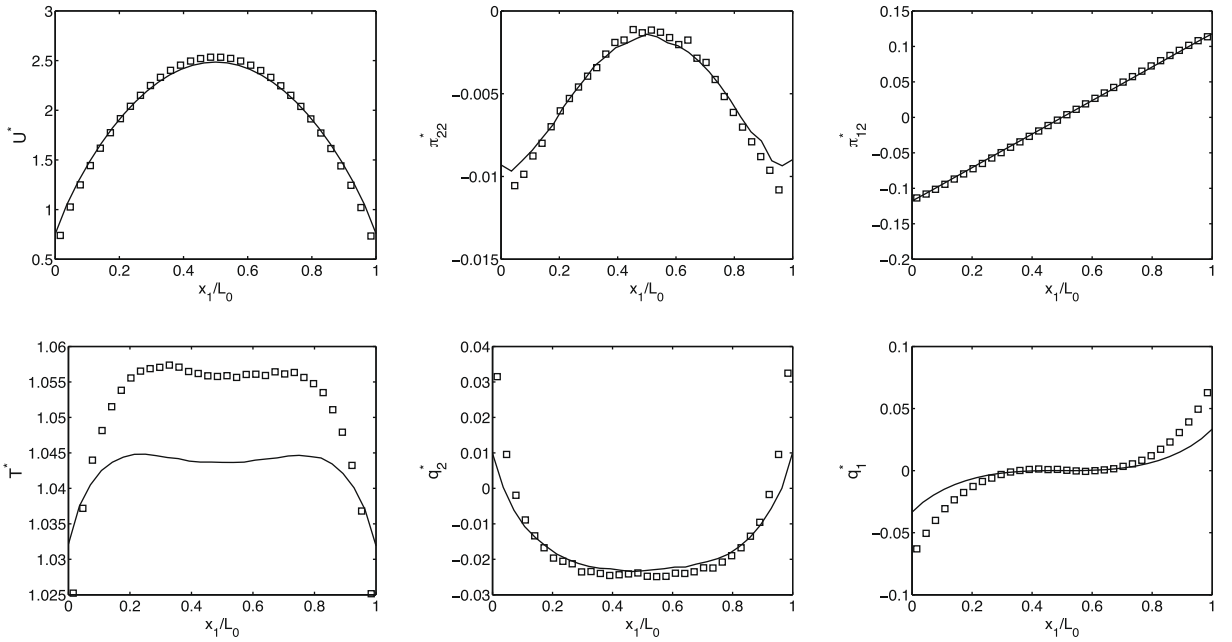

Fig. 11. Detailed comparison between the Fokker–Planck model (symbols) and DSMC (lines) for $Kn = 0.072$: depicted are the normalized profiles of U_2^{ast} (top left), π_{22}^{ast} (top middle), π_{12}^{ast} (top right), T^{ast} (bottom left), q_2^{ast} (bottom middle) and q_1^{ast} (bottom right).

Table 1
Grid convergence: $J/J^{converged}$ for $Kn = 5.3$ calculated with the new Fokker–Planck model on grids with 64, 32, 16, 8 and 4 cells.

Number of grid cells	$J/J^{converged}$
64	1.000
32	1.002
16	1.009
8	1.020
4	1.052

Table 2
Grid convergence for the 2D test case.

Number of grid cells	Δt	$J/J^{converged}$
64×64	0.075τ	1.000
32×32	0.15τ	1.027
16×16	0.3τ	1.046
8×8	0.6τ	1.051

cylinder of diameter $L_0/2$ at its center (shown in Fig. 12 together with computational particles and a 32×32 grid). The temperature of the body and the vertical walls is kept constant at T^{wall} and periodic boundary conditions are applied at the top and bottom confinements. The flow is driven by an external force directed downwards. To estimate $\boldsymbol{U}$ and e_s, a structured grid, which is non-conforming with the cylinder geometry, is employed. For all simulations, $Kn = \lambda/(0.25L_0) = 2\sqrt{RT^{wall}}\tau/L_0 = 0.1$, $\widehat{F} = FL_0/(RT^{wall}) = 0.4$ and $\Delta t = 0.24h/u_{rms}$ were used. The values of the dimensionless mass flux $J/J^{converged}$ computed with the new particle time stepping scheme using 64×64, 32×32, 16×16 and 8×8 grids with 10 computational particles per cell are presented in Table 1 (here, $J^{converged}$ represents the value obtained for a grid with 64×64 cells). In all cases a time averaging factor n_a of 10,000 was employed. Note that the methodology can also be applied for unsteady problems, but in that case instead of time averaging the number of particles has to be increased. Corresponding vector plots with Mach contours are depicted in Fig. 13. It is remarkable how insensitive the results are with respect to grid resolution (to obtain the result shown in Fig. 13(d) only $8 \times 8 \times 10 = 640$ particles were employed). In some sense this is not too surprising, since the particles always interact with the analytical cylinder geometry and since convection is independent

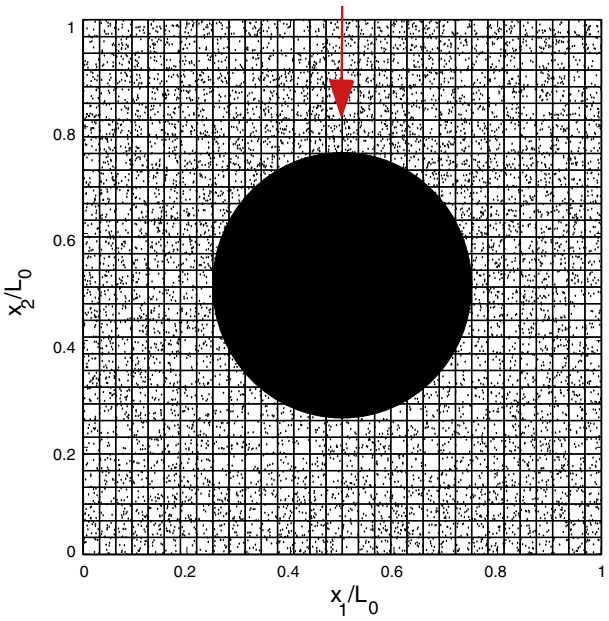

Fig. 12. Domain of 2D test case with grid, cylindrical body and computational particles. Also shown is the 32×32 grid, which is employed to estimate and interpolate $\boldsymbol{U}$ and e_s. The flow is directed from top to bottom and x_1 is the distance from the left wall.

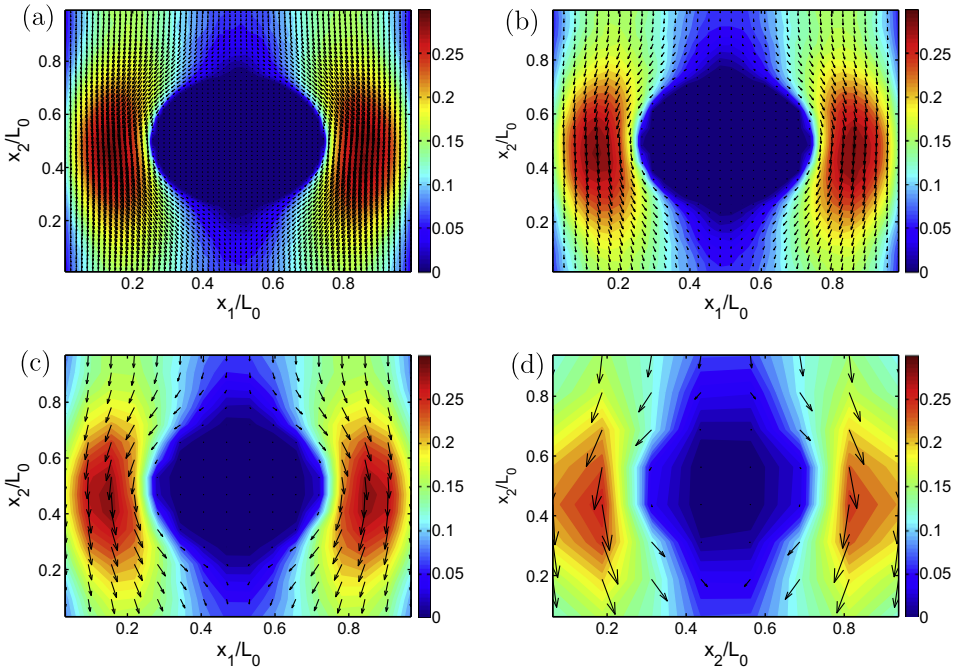

Fig. 13. 2D test case: velocity vectors and Mach contour lines. The plots (a), (b), (c) and (d) show the result obtained with the new particle time stepping scheme using 62×64, 32×32, 16×16, 8×8 grids, respectively. In all cases, the time step size was $\Delta t = 0.24\ h/u_{rms}$.

of the grid resolution; it is only the local estimation of $\boldsymbol{U}$ and e_s, which relies on a grid. It can be expected that the influence of the grid resolution becomes even weaker for larger Knudsen numbers. To confirm that a time step size of $\Delta t = 0.24\ \mathrm{h}/u_{rms}$ is small enough, an additional simulation with $\Delta t = 0.12\ \mathrm{h}/u_{rms}$ and a grid with 32×32 cells was performed; the difference between the corresponding mass fluxes is of the same order as the statistical error (in the order of 1%).

To demonstrate the influence of the particle time stepping scheme on the energy balance, temperature contour plots calculated with the new scheme (Section 4.2) and with the standard second order discretization schemes (77) and (78) are

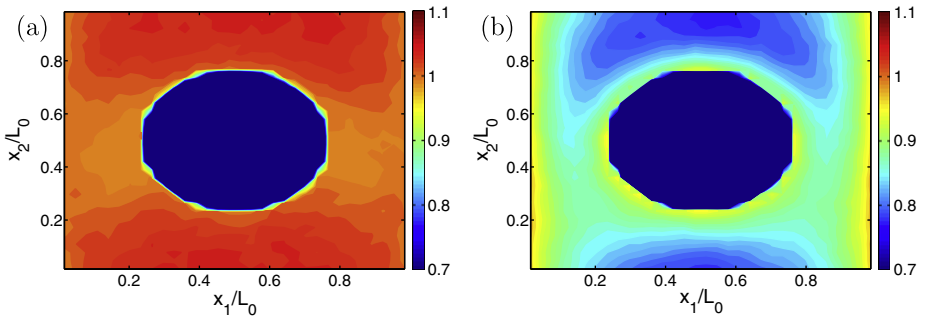

Fig. 14. 2D test case: temperature surface plots. The surface plots (a) and (b) show the normalized temperature field computed with the new and the standard schemes, respectively. In both cases, the same 32×32 grid was used and the time step size was $\Delta t = 0.24\ \mathrm{h}/u_{rms} = 0.15\tau$.

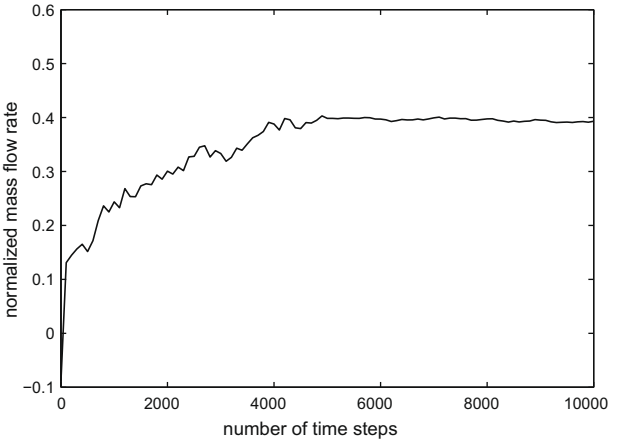

Fig. 15. Convergence to statistical steady state for the new scheme: shown is the normalized mass flow rate $\widehat{J}/\widehat{F}$ for the 2D test case with a 32×32 grid as a function of the number of time steps. The time step size was $\Delta t = 0.24\ \mathrm{h}/u_{rms} = 0.15\tau$; for the first 5000 time steps the time averaging factor was $n_a = 100$ and from then on $n_a = 1000$ was used.

shown in Fig. 14. In both cases a 32×32 grid with 10 particles per cell, $\Delta t = 0.24\ \mathrm{h}/u_{rms} = 0.15\tau$ and $n_a = 10,000$ were employed. Despite the relatively small time step size (compared to the time scale τ), it can clearly be observed that the standard scheme leads to a significant, unphysical cooling of the gas, which becomes prominent away from the walls. With the new scheme, on the other hand, a slight increase of the temperature away from the walls (dissipated energy) is predicted, which is what we expect. This result is in agreement with our isolated studies presented in Fig. 1. Note that the numerical artifact resulting from the time integration with the standard scheme becomes bigger for larger time steps or smaller Knudsen numbers. Finally, Fig. 15 shows convergence to steady state for the 2D test case with the new time stepping scheme, i.e. the normalized mass flow rate $\widehat{J}/\widehat{F}$ as a function of the number of time steps. For the first 5000 time steps the time averaging factor was $n_a = 100$ and from then on $n_a = 1000$ was used. One can see that statistical steady state is reached after approximately 6000 time steps. Note, however, that this depends on Kn, Ma, the number of particles per grid cell and on the time averaging factor n_a. For this convergence study, 10 particles per cell were employed. Although no attempt has been made to optimize the performance of our $C++$ simulator, we want to mention that running 3000 time steps takes approximately one minute on a MacBookPro (on one core). Depending on the level of statistical error one is willing to accept, more computational time is required for time averaging.

6. Conclusion

This paper introduces and discusses a new simulation tool for non-equilibrium gases, based on the integration of a stochastic velocity model for the paths of representative gas particles. It can be viewed from different perspectives: The stochastic differential equations model gas particles directly on the microscopic level allowing for various physical extensions. The stochastic model can also be shown to correspond to a kinetic Fokker–Planck equation, which in turn is an approximation to the full Boltzmann equation for rarefied gases. At last, the model can be viewed as a modification of the Direct Simulation Monte-Carlo (DSMC) approach for non-equilibrium gases, where the efficiency is increased by replacing pair-wise collisions with special stochastic noise, loosing only little physical accuracy.

In the case of small relaxation times, the stochastic model has been shown to approximate standard compressible fluid dynamics for monatomic gases including viscosity and heat conduction with a Prandtl number of 3/2. For larger relaxation times, the model describes non-standard kinetic effects, like the Knudsen paradox. Refined models can be extended for consistent Prandtl numbers and complex molecules.

In the second part of the paper, an efficient and accurate integration technique for the resulting stochastic equations is devised. We make use of exact integration and correlation to present a scheme that exactly preserves the excess energy in equilibrium independent of the time step size. This is an important property to guarantee correct temperature fields when computing fluid flows. In the integration, the time step becomes unrestricted with respect to the collision scale. Various numerical experiments demonstrate the capabilities of the new model and integration technique. Future work includes further validation of the Fokker–Planck model for large Knudsen numbers and detailed comparisons with DSMC results.

References

[1] G. Abbate, C.R. Kleijn, B.J. Thijsse, Hybrid continuum/molecular simulations of transient gas flows with rarefaction, AIAA J. 47 (7) (2009).
[2] M.S. Anand, A.T. Hsu, S.B. Pope, Calculations of swirl combustors using joint velocity-scalar probability density function method, AIAA J. 35 (7) (1997) 1143–1150.
[3] C. Beck, G. Roepstorff, From stochastic processes to the hydrodynamic equations, Physica A 165 (2) (1990) 270–278.
[4] P.L. Bhatnagar, E.P. Gross, M. Krook, A model for collision processes in gases. I. Small amplitude processes in charged and neutral one-component systems, Phys. Rev. 94 (1954) 511–525.
[5] G.A. Bird, Molecular Gas Dynamics and the Direct Simulation of Gas Flows, Clarendon Press, Oxford, 1994.
[6] C. Cercignani, The Boltzmann Equation and its Application, Springer-Verlag, New York, 1988.
[7] B.J. Delarue, S.B. Pope, Application of PDF methods to compressible turbulent flows, Phys. Fluids 9 (9) (1997) 2704–2715.
[8] W. Dong, From stochastic processes to the hydrodynamic equations, University of California Report No. UCRL-3353, 1956.
[9] S. Heinz, Statistical Mechanics of Turbulent Flows, Springer-Verlag, Berlin, 2003.
[10] S. Heinz, Molecular to fluid dynamics: the consequences of stochastic molecular motion, Phys. Rev. E 70 (3) (2004) 036308.
[11] S. Heinz, Unified turbulence models for LES and RANS, FDF and PDF simulations, Theor. Comp. Fluid Dyn. 21 (2) (2007) 99–118.
[12] P. Jenny, M. Muradoglu, K. Liu, S.B. Pope, D. Caughey, Pdf simulations of a bluff-body stabilized flow, J. Comput. Phys. 169 (1) (2001) 1–23.
[13] P. Jenny, S.B. Pope, M. Muradoglu, D. Caughey, A hybrid algorithm for the joint pdf equation of turbulent reactive flows, J. Comput. Phys. 166 (2) (2001) 218–252.
[14] J.G. Kirkwood, The statistical mechanical theory of transport processes. 1. General theory, J. Chem. Phys. 14 (3) (1946) 180–201.
[15] J.G. Kirkwood, F.P. Buff, M.S. Green, The statistical mechanical theory of transport processes. 3. The coefficients of shear and bulk viscosity of liquids, J. Chem. Phys. 17 (10) (1949) 988–994.
[16] M. Knudsen, Die gesetze der molekularstrmung und der inneren reibungsstrmung der gase durch rhren, Ann. Phys. 333 (1909) 75–130.
[17] J.L. Lebowitz, H.L. Frisch, E. Helfand, Nonequilibrium distribution functions in a fluid, Phys. Fluids 3 (3) (1960) 325–338.
[18] A.R. Masri, S.B. Pope, PDF calculations of piloted turbulent non-premixed flames of methane, Combust. Flame 81 (1) (1990) 13–29.
[19] D.W. Meyer, P. Jenny, Consistent inflow and outflow boundary conditions for transported probability density function methods, J. Comput. Phys. 226 (2) (2007).
[20] L. Mieussens, Discrete-velocity models and numerical schemes for the Boltzmann–BGK equation in plane and axisymmetric geometries, J. Comput. Phys. 162 (2000) 429.
[21] J.-P. Minier, J. Pozorski, Analysis of a PDF model in a mixing layer case, in: Tenth Symposium on Turbulent Shear Flows, 1995, 26.25–26.30.
[22] P.A. Nooren, H.A. Wouters, T.W. J Peeters, D. Roekaerts, U. Maas, D. Schmidt, Monte Carlo PDF simulation of a turbulent natural-gas diffusion flame, Proc. Combust. Inst. 26 (1996) 272.
[23] T. Ohwada, Y. Sone, K. Aoki, Numerical analysis of the poiseuille and thermal transpiration flows between two parallel plates on the basis of the boltzmann equation for hard spheres molecules, Phys. Fluids A 1 (1989) 2042–2049.
[24] S.B. Pope, Turbulent Flows, Cambridge University Press, Cambridge, 2000.
[25] B. Rembold, P. Jenny, A multiblock joint pdf finite-volume hybrid algorithm for the computation of turbulent flows in complex geometries, J. Comput. Phys. (2006).
[26] V. Saxena, S.B. Pope, PDF calculations of major and minor species in a turbulent piloted jet flame, Proc. Combust. Inst. 27 (1998) 1081–1086.
[27] H. Struchtrup, Macroscopic Transport Equations for Rarefied Gas Flows, Springer-Verlag, New York, 2005.
[28] H. Struchtrup, M. Torrilhon, Regularization of Grad's 13-moment-equations: derivation and linear analysis, Phys. Fluids 15 (2003) 2668–2680.
[29] S. Succi, The Lattice Boltzmann Equation, Oxford University Press, Oxford, 2001.
[30] M. Torrilhon, H. Struchtrup, Boundary conditions for regularized 13-moment-equations for micro-channel-flows, J. Comput. Phys. 227 (2008) 1982–2011.
[31] D.A. Wolf-Gladrow, Lattice Gas Cellular Automata and Lattice Boltzmann Models, Springer, 2000.
[32] R.W. Zwanzig, J.G. Kirkwood, I. Oppenheim, B.J. Alder, The statistical mechanical theory of transport processes. 7. The coefficients of thermal conductivity of monatomic liquids, J. Chem. Phys. 22 (5) (1954) 783–790.
[33] R.W. Zwanzig, J.G. Kirkwood, K.F. Stripp, I. Oppenheim, The statistical mechanical theory of transport processes. 6. A calculation of the coefficients of shear and bulk viscosity of liquids, J. Chem. Phys. 21 (11) (1953) 2050–2055.